Life Cycle and Precipitation Formation in a Hybrid-Type Hailstorm Revealed by Polarimetric and Doppler Radar Measurements

H. HÖLLER,* V. N. BRINGI,** J. HUBBERT,** M. HAGEN,* AND P. F. MEISCHNER*

*Institute of Atmospheric Physics, DLR-Oberpfaffenhofen, Wessling, Germany
**Department of Electrical Engineering, Colorado State University, Fort Collins, Colorado

ABSTRACT

Hailstorm processes are studied using multiparameter radar observations of thunderstorm evolution. The storm turned out to be of hybrid type, having both multicellular (oscillatory nature of hail production) and supercellular (quasi-steady state of basic dynamics) characteristics. Its reflectivity field showed a V-like pattern not yet described in the literature as a typical severe storm pattern. The flow was characterized by an updraft zone surrounding an embedded downdraft collocated with the main precipitation shaft.

The precipitation mainly originated from graupel particles growing at the fringes of the main updraft zone, whereas an accumulation zone of big drops was not present. In the weaker parts of the updraft the falling graupel melted and reached the ground as rain, whereas in the main updraft region those raindrops could be recirculated and subsequently freeze or be captured by hailstones already present aloft. In this region of high liquid water content large hail could be grown; it fell out in the main downdraft region immediately beside the main updraft zone. Comparison of the radar-derived hailswath and ground observations of hail damage gave encouraging verification of the LDR-Z_{DR} hail signature defined in this paper.

1. Introduction

The microphysical processes leading to the growth of large hail in thunderstorms as well as the associated dynamics have been of great interest in experimental as well as numerical studies performed in the last decade.

A major objective of the field experiments was testing of hypotheses and methods for artificially modifying the hail process in order to prevent large damaging hail at the ground. The existence of an accumulation zone of large supercooled drops in a hailstorm was first hypothesized by Sulakvelidze (1969). After freezing, these drops should act as embryos for hail growth. Seeding these zones with artificial ice nuclei (mostly silver iodide) was supposed to accelerate the freezing process by producing a large number of hailstone embryos nearly simultaneously. These were assumed to subsequently compete for the remaining liquid water, resulting in more but smaller hailstones than would have occurred without seeding (competition hypothesis).

This hypothesis has been tested in randomized field experiments such as Grossversuch IV in Switzerland (Federer et al. 1986) and the National Hail Research

Experiment (NHRE) in Colorado (Knight et al. 1979). In both studies, no significant effects of the seeding operations could be found. The underlying hypotheses were shown to be invalid. In NHRE it turned out that the hailstone embryos were mainly graupel particles. Although about half of the embryos were frozen drops in the Swiss storms, it was argued from a series of aircraft penetrations that an accumulation zone of supercooled raindrops did not exist (Waldvogel et al. 1987).

The development of multiparameter radar techniques made it possible to discriminate ice phase from liquid phase hydrometeors. The differential reflectivity (Z_{DR}) is a measure of the difference of the echoes for horizontal and vertical polarized radiation. It is indicative of oblate raindrops and has been introduced by Seliga and Bringi (1976) for rain rate estimation. Combining reflectivity and differential reflectivity, Aydin et al. (1986) derived a hail signal function (H_{DR}). The hail probability increases with increasing reflectivity (larger particle size) as well as with decreasing Z_{DR} (spherical or tumbling hailstones). Bringi et al. (1986a) found their computations of linear depolarization ratio (LDR) for graupel particles to fit the radar measurements in convective clouds reasonably well. Hail size has been inferred by Balakrishnan and Zrnić (1990b) by measurements of cross-correlation between orthogonally polarized radiation. Hail was further characterized by Steinhorn and Zrnić (1989) using specific differential phase (K_{DP}).

Corresponding author address: Dr. Hartmut Höller, Institute of Atmospheric Physics, DLR—Oberpfaffenhofen, Postfach 11 16, D-82230 Wessling, Germany.

The microphysical characteristics of hailstorms are closely related to the dominant dynamical processes. Foote (1985) presented a thunderstorm classification with special focus on the hail processes. The dynamical aspects were taken into account by structural and evolutionary aspects of the storms. The number of cells (unicellular or multicellular), cell lifetime, evolutionary patterns, and the organization of cells have been used as ordering criteria. As a further refinement of the classification scheme, the source of hailstone embryos has been introduced. In a detailed case study of a Colorado hailstorm (Foote and Wade 1982; Heymsfield and Musil 1982; Foote and Frank 1983), the radar echo evolution, particle growth processes, and the airflow were studied for a hailstorm that had some common features with the storm investigated in this paper. We present radar polarimetric measurements for a hailstorm together with single-Doppler measurements and, for the first time, discuss these data in the context of hailstorm types and processes. Thereby, additional insights into the microphysics of hail growth are obtained. A hydrometeor classification scheme based on Z_{DR} and LDR is suggested, which is supported by scattering computations. The radar data are further compared with ground observations of hailfall. The measurements were performed in summer 1990 by the polarization diversity radar (POLDIRAD) (see Schroth et al. 1988) of DLR located in southern Germany.

Using numerical experiments Weisman and Klemp (1982) have studied thunderstorm development under different environmental conditions of buoyancy and wind shear. A spectrum of storm types as inferred by observations could be reproduced. Supercellular storms found their model equivalent in the split-storm regime, whereas the multicellular counterparts were simulated by secondary storm evolutions. An examination of the large-scale environment for the case studied here is used to characterize the storm in the context of existing classification schemes and to compare it with detailed case studies of similarly typed storms.

2. The storm environment

For analyzing the storm environment we confine ourselves primarily to conventionally available meteorological data. Additional information on the local low-level winds is provided by the radar-derived wind profile using velocity azimuth display (VAD) analysis (Browning and Wexler 1968).

The general synoptical situation was characterized by a moderate southwesterly flow aloft associated with the eastern flank of a low pressure trough approaching the observational area (southern Germany) from the west. Under these circumstances synoptic-scale lifting may help to destabilize the atmospheric stratification in connection with the differential advection mechanism (e.g., Barnes and Newton 1986). In accordance with this model the storm discussed in this paper occurred

in the warm sector air mass ahead of a cold front passing the observation site later at night associated with a squall-line type of convective organization.

The main alpine ridge is roughly west–east oriented at about 100 km south of the radar site. Under this configuration, a lee cyclone had developed north of the Alps, giving rise to easterly low-level winds in this region. With stronger gradient winds aloft, foehn situations may result from this kind of flow, especially in wintertime, as described by Hoinka and Rösler (1987).

This situation is especially favorable for the development of severe storms, as it produces (i) a great thermal instability and (ii) strong wind shear accompanied by a veering of the wind and shear vectors with height, as can be seen from Figs. 1 and 2. The 1200 UTC (1400 local time) sounding at Munich is shown here. The wind profile is a composite of the radio sounding and a VAD radar analysis for the lowest 2.8 km above ground, which had been taken closer to the storm when it passed north of the radar site. The shear conditions shown here also turned out to be typical for Alberta hailstorms (Chisholm and Renick 1972). The sounding (Fig. 1) shows that only a shallow surface layer is humid enough to initiate cumulus clouds. The lifting condensation level is at 1.66 km MSL, which corresponds to 1.06 km AGL (above ground level) at the radar site (600 m MSL). Cloud base at this level is rather warm (15.2°C) and humid (12.9 g kg^{-1} water vapor mixing ratio). At about 2.5 km MSL a shallow stable layer is capping the boundary-layer air. This level also coincides with the rapid change of the more or less continuously veering wind vector in the lowest 1.9 km AGL. This is not an artifact arising from the composition of the wind profile from radar and radiosonde data. At higher levels the air is much drier, especially between
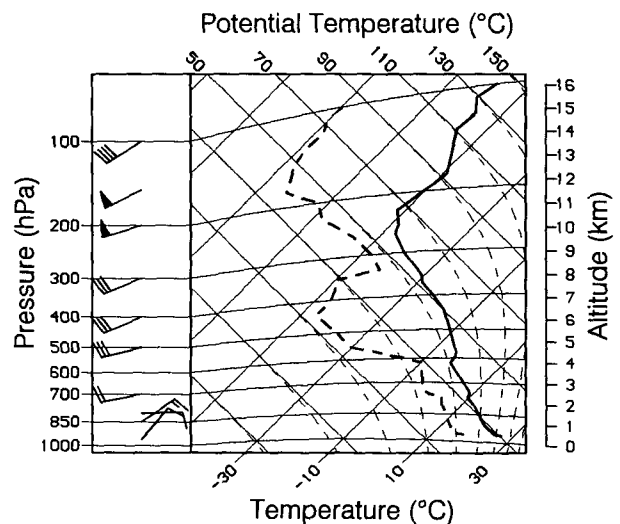

FIG. 1. The 1200 UTC 30 June 1990 sounding at Munich. Temperature (solid line) and dewpoint (dashed line) are shown. Wind barbs are indicated on the left margin.
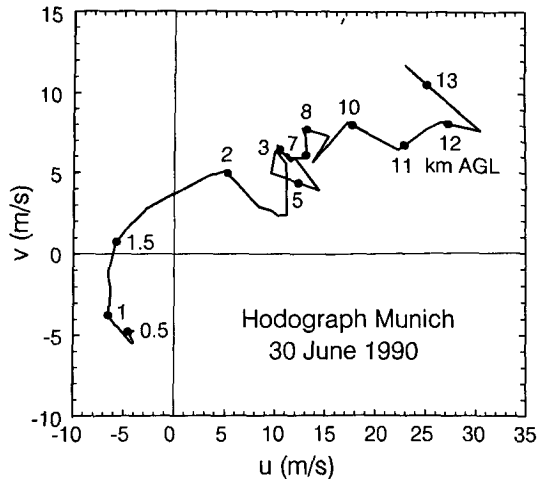
FIG. 2. Composite hodograph constructed from a VAD radar scan at 1544 UTC used for the lowest 3 km AGL and the Munich sounding taken for the higher levels. Dots mark indicated heights in kilometers.

4 and 8 km MSL. Wind velocities are generally increasing slowly, whereas the direction is approximately southwest at all heights above 2 km AGL.

Weisman and Klemp (1982) have characterized the formation of different types of storms for various initial conditions by a bulk Richardson number R, defined as a buoyancy-to-shear ratio. The environmental conditions for the storm studied in this paper lead to $R = 41$ for the modified wind profile (as shown in Fig. 2) and to $R = 47$ for the original sounding of Munich. In these calculations, the buoyancy term has been assessed from the lifting condensation level. Using mean values for the lowest 500 m above ground (as applied by Weisman and Klemp 1982) results in a Richardson number of 12 because buoyancy is reduced considerably by the strong humidity gradient at the ground. Such a profile probably is not representative for the storm observed, as cloud development would have been suppressed according to the large negative buoyancy extending to heights up to 1 km above cloud base.

Thus, $R = 41$ seems to be the most consistent and, consequently, the most probable value that can be derived from conventional data. This places the storm in the transitional region from supercell or split storms with small Richardson numbers to the secondary or multicell storms with larger R. As will be discussed in the following sections in more detail, the storm had features characteristic of both regimes. It may be termed a hybrid storm, comparable to the cases described by Nelson and Knight (1987), Nelson (1987), and Foote and Frank (1983).

3. The general evolution of the storm

The storm development can be characterized by three phases: 1) the initialization phase, which lasts

roughly until 1315 UTC, 2) the mature phase, from 1315 to 1455 UTC, and 3) the decaying phase.

The storms were initialized about 120 to 160 km WNW of the radar site over hilly terrain of the Schwäbische Alb. The first cells formed a line configuration of ordinary storms oriented along the mountain ridge from SW to NE. At 1253 UTC the reflectivity pattern shows four main centers (cells A to D, Fig. 3). The direction of propagation is basically from the WSW, which corresponds to the direction of the midlevel winds. At about 1258 UTC the cores of cells C and D merge and continue their propagation as a common echo mass, whereas cells A and B decrease in intensity and dissipate.

At 1315 UTC the reflectivity pattern has changed substantially. A weak echo region (WER or W in Fig. 3) has formed SE of the reflectivity center. The WER is bounded (BWER) by a ring of reflectivity values that are lower than those represented in Fig. 3. The direction of storm propagation as shown in Fig. 4 deviates to the right of the midlevel winds. This deviation increases progressively with time rather than changing abruptly with the appearance of the WER. A 40° shift to the right of the initially WSW direction can be seen for the period from 1300 to 1500 UTC, which is just between the 30° to 50° deviation found by Chisholm and Renick (1972) for multicell and supercell storms, respectively. The storm speed as determined from the reflectivity maximum of consecutive PPI scans does not show a clear tendency but is characterized by large fluctuations. This might be caused by different cell centers accounting for the actual location of the maximum reflectivity, thus reflecting the storm's internal unsteadiness. A pronounced hook echo at lower levels cannot be found for this storm. This indicates that the storm did not develop a large mesocyclone, as is typical for supercell storms. The circulation of the storm will be discussed in more detail in the next section. An interesting feature in this stage of development is the V-like reflectivity pattern, which is most clearly seen from the 50-dBZ contour in the 1447 UTC PPI (Fig. 3).

At about 1500 UTC the storm began to decay. The BWER had considerably weakened at 1509 UTC.

4. The storm's flow field

For deriving the airflow pattern of the storm, we (i) track individual radar reflectivity maxima on their way through the storm system and (ii) use the single-Doppler measurements. These data enable us to construct a conceptual model of the storm's flow field. Thereby it is possible to describe the polarimetric features in the context of storm dynamics.

Storm development will be discussed during the time where the most extensive polarimetric measurements have been made. These include "time series" scans (see Schroth et al. 1988) performed at 1438 and 1457 UTC. Specifically, we discuss cell tracks from just before the time series scans.
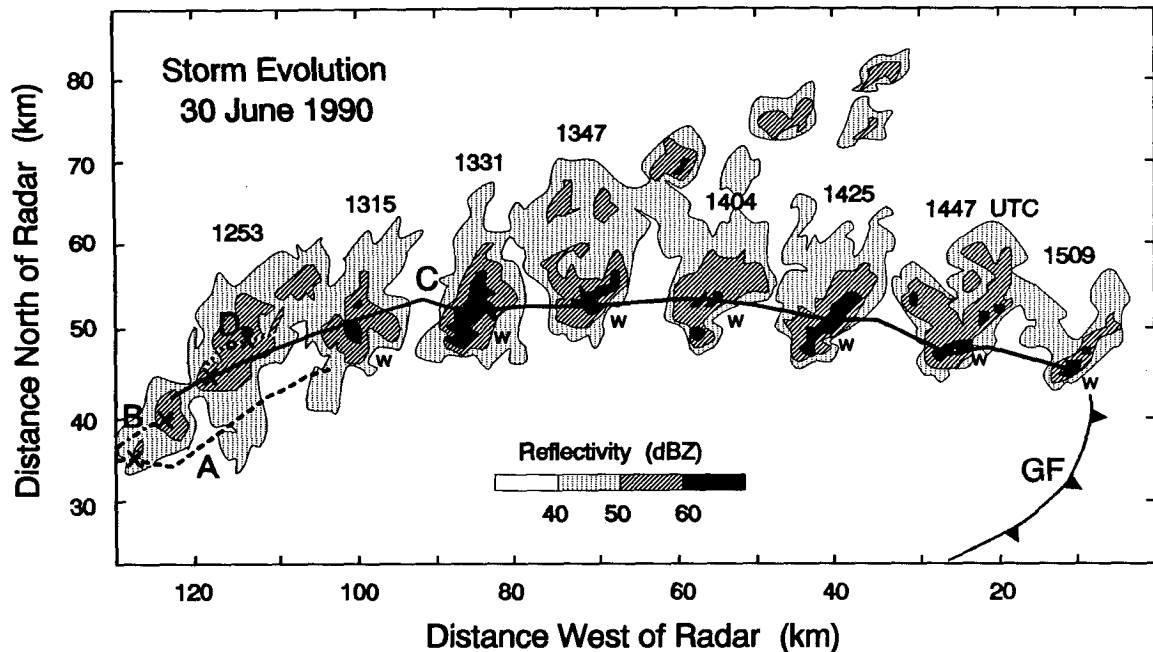
FIG. 3. Evolution of the storm's reflectivity pattern: 40-, 50-, and 60-dBZ contours are shown for different times at those elevations demonstrating most clearly the weak echo structure (W). Tracks of four different reflectivity centers (A to D) at 2.2° elevation as well as their position at 1253 UTC (×) are indicated. The position of the gust front G as marked by a thin line echo at 1509 UTC is also indicated.

The storm-relative tracks of six different cells are shown in Fig. 5. A cell is defined by the echo mass within a closed contour of radar reflectivity containing a local reflectivity maximum. We note three principal paths: 1) cells 1 and 2 are traveling from south to north on the rear (western) flank, 2) cell 3 representing the main storm core is following an anticyclonic path, and 3) cells 4, 5, and 6 move south–north on the front (eastern) storm flank. From Fig. 6 we see cells 1 and 2 in a decaying stage. The reflectivity maxima decrease in intensity as they descend to the ground. Cell 3 is also slowly descending, but its reflectivity does not decrease substantially. It corresponds to the storm's main precipitation fallout. Cells 4, 5, and 6 are in their developing stage, as can be seen from the generally increasing reflectivity values. The height of the maxima between 7 and 8 km is also indicative of developing precipitation, whereas cells 1, 2, and 3 are found at substantially lower levels.

This general flow pattern is substantiated by the distribution of the radial velocities as obtained from the single-Doppler measurements. From these fields areas of radial convergence and divergence can be identified as possible regions of updrafts or downdrafts. Furthermore, a rotational flow is indicated by azimuthal shear. Supplementary information was provided by visual observation of the storm. New cell growth and an overshooting cloud top were noted on the southern flank as well as an anvil extending into northerly directions.

To describe the airflow in a storm-relative framework the mean storm velocity of 11.4 m s^{-1} from 285° is subtracted from the ground-relative values. Figure 7 shows the storm-relative Doppler velocities for three different elevation angles and for a vertical section at constant azimuth. Selected reflectivity contours have
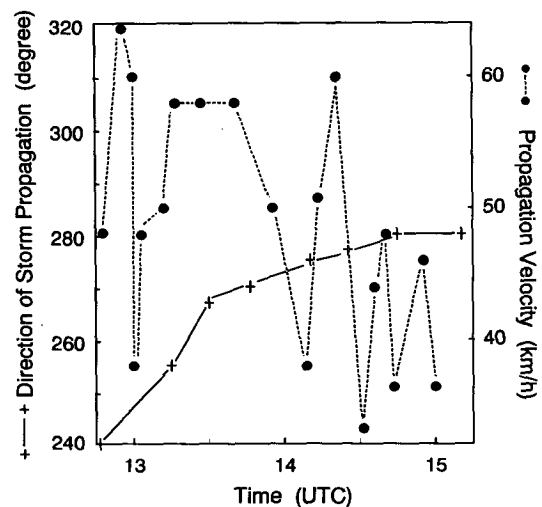

FIG. 4. Speed and direction of storm propagation. Solid line shows the direction from which the storm (center of cell C) is moving. Dashed line shows storm speed.
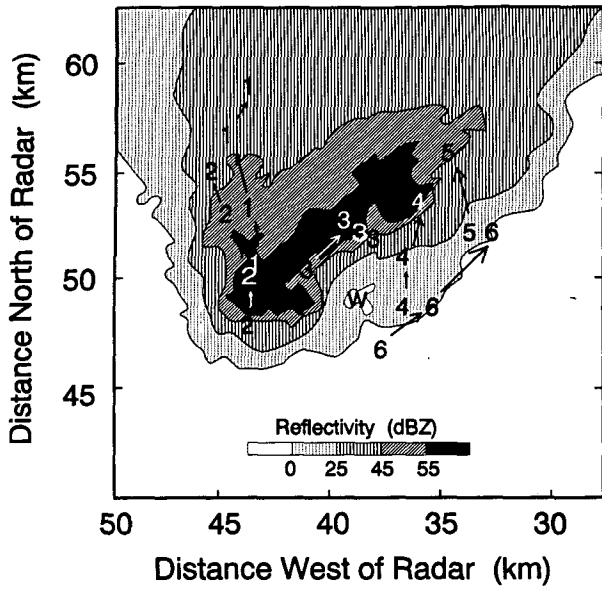
FIG. 5. Storm-relative tracks of six different cells during the period from 1424 to 1436 UTC. The storm-relative positions of the reflectivity maxima are shown as a horizontal projection. Radar reflectivity contours for 1424 UTC at a height of 6 km are superimposed. The bounded weak echo region is marked by W.

been superimposed. The arrows indicate possible streamlines consistent with the velocity measurements.

The low-level flow (Fig. 7a) is characterized by anticyclonic rotation in the southern parts of the storm. Positive velocities (away from the radar) are found in the western parts with maximum values at the southwestern edge. This picture is in accordance with the south-to-north movement of cells 1 and 2. Negative velocities prevail in the central parts of the radar echo with a minimum at the southeastern edge partly coinciding with the high-reflectivity core (>60 dBZ) and

extending into the region of strong reflectivity gradient. The motion of cell 3 supports this anticyclonic rotation within the high-reflectivity center. The vertical section in Fig. 7d along line A–B suggests that this region is the main downdraft area. The largest negative velocities may be connected to the deflection of the downdraft at the ground contributing to the low-level outflow circulation. Positive values of radial velocity are found at the eastern flank of the storm. This is in accordance with the lower parts of cells 4, 5, and 6 traveling to the NNE.

At midlevels (Fig. 7b), the main flow features are still quite similar to those at low levels except that (i) the anticyclonic rotation in the high reflectivity zone has weakened, (ii) a weak echo region (WER) is present at the southeastern edge of the storm, and (iii) cyclonic rotation can be seen at the southeastern edge of the WER. Most probably, the WER is the location of the main updraft. Because of the high updraft speeds not many precipitation particles are found in this zone. The southeastern part of the WER is characterized by a small center of cyclonic vorticity.

At upper levels (Fig. 7c) the flow is characterized by a diverging pattern with an embedded smaller-scale rotational feature. Its position is directly on top of the WER and possibly marks the location of the main updraft.

Thus, the cell development as well as the flow structure discussed so far suggest a region of growing cells associated with updrafts around the southern periphery of the storm. The main updraft is probably located at the southeastern storm flank within the WER. Most of the precipitation growing at its fringes and top does not penetrate down to the 5-km level. Moreover, it is carried around the main updraft at the storm's western (cells 1 and 2) and eastern (cells 4, 5, and 6) flanks, or it is crossing the main updraft core at higher levels and subsequently falling down close to the updraft core
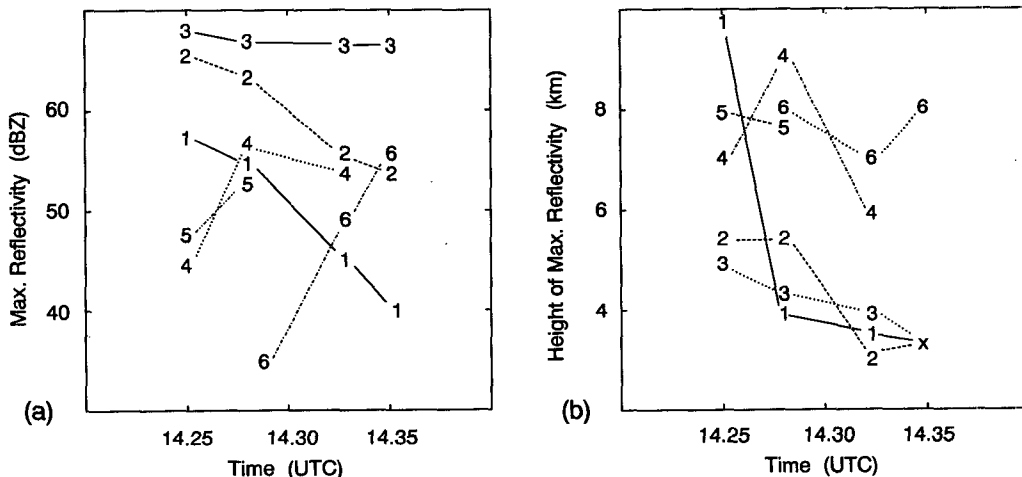

FIG. 6. Maximum radar reflectivity (a) and its height above ground (b) for the cells shown in Fig. 5.
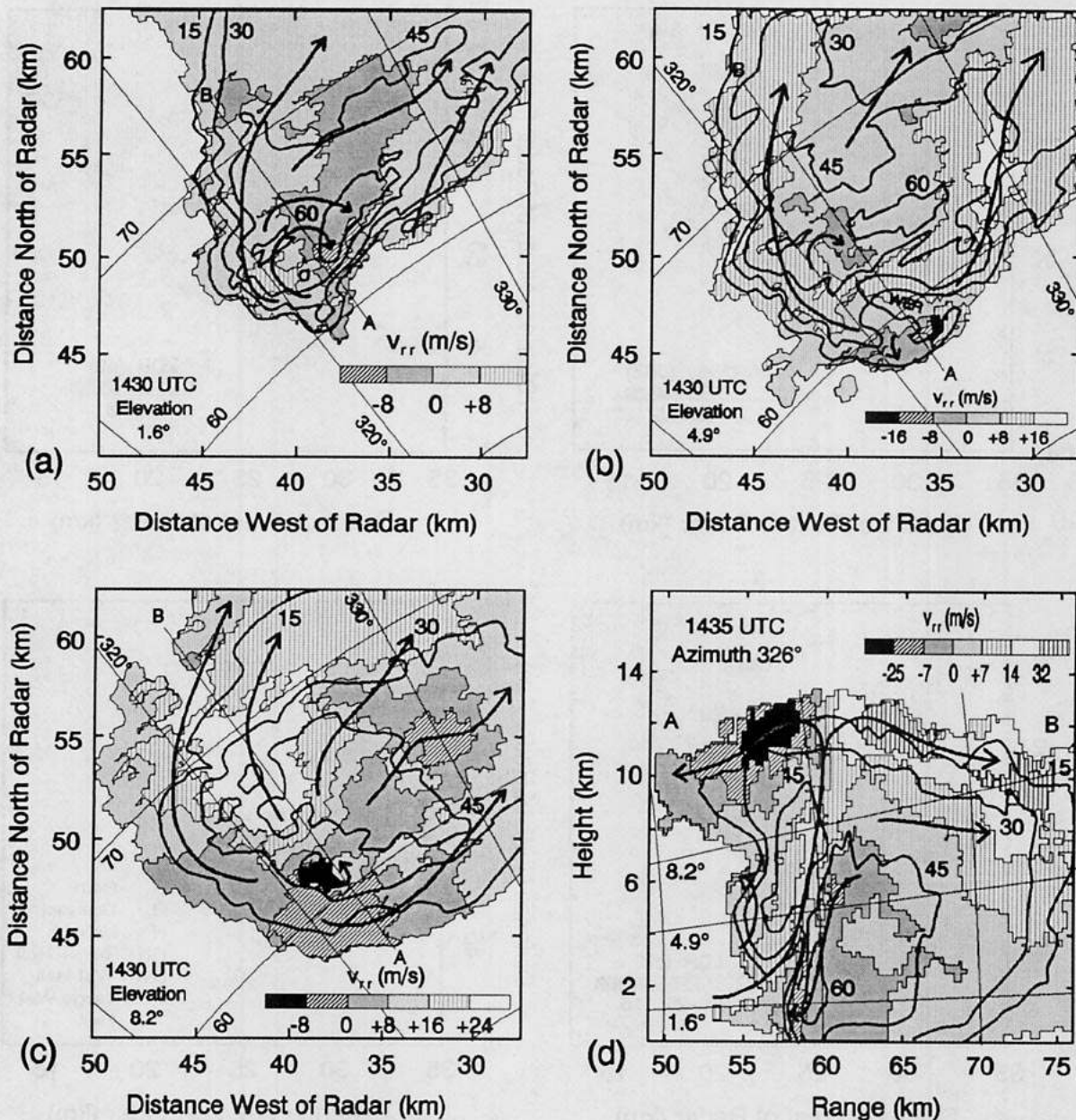
FIG. 7. Storm-relative Doppler (radial) velocity v_{rr} (shaded areas), reflectivity contours (solid lines) labeled in dB, and possible streamlines (solid arrows) as suggested by the v_{rr} field. A radar-centered spherical coordinate system is shown as an overlay. Radial distances are indicated in km. Storm scans at 1430 UTC are shown at different elevation angles of (a) 1.6°, (b) 4.9°, and (c) 8.2°. In (d) a vertical section taken at 1435 UTC is presented. Taking into account the storm advection, the vertical scan corresponds to a section along A–B in (a)–(c).

at its northwestern side (cell 3). These principal patterns are similar to those found by Browning and Foote (1976) for the Fleming storm.

Regardless of the cellular character of the storm, the low- and midlevel radar echo exhibits a persistent V-shaped structure. It is clearly seen from the 45-dBZ contour line in Figs. 7a and 7b. The echo is likely to be produced by the cells traveling from south to north on both sides of the storm. Attenuation effects cannot

explain the V-shaped reflectivity pattern because the orientation of the V is mostly such that the reflectivity decreases and subsequently increases again with range (e.g., Fig. 8).

The flow structure shown in Fig. 7 is only a snapshot in the overall storm development, but many features remain essentially unchanged, at least during the half-hour of observation time to be discussed in the following. Some small-scale features have more or less a transient
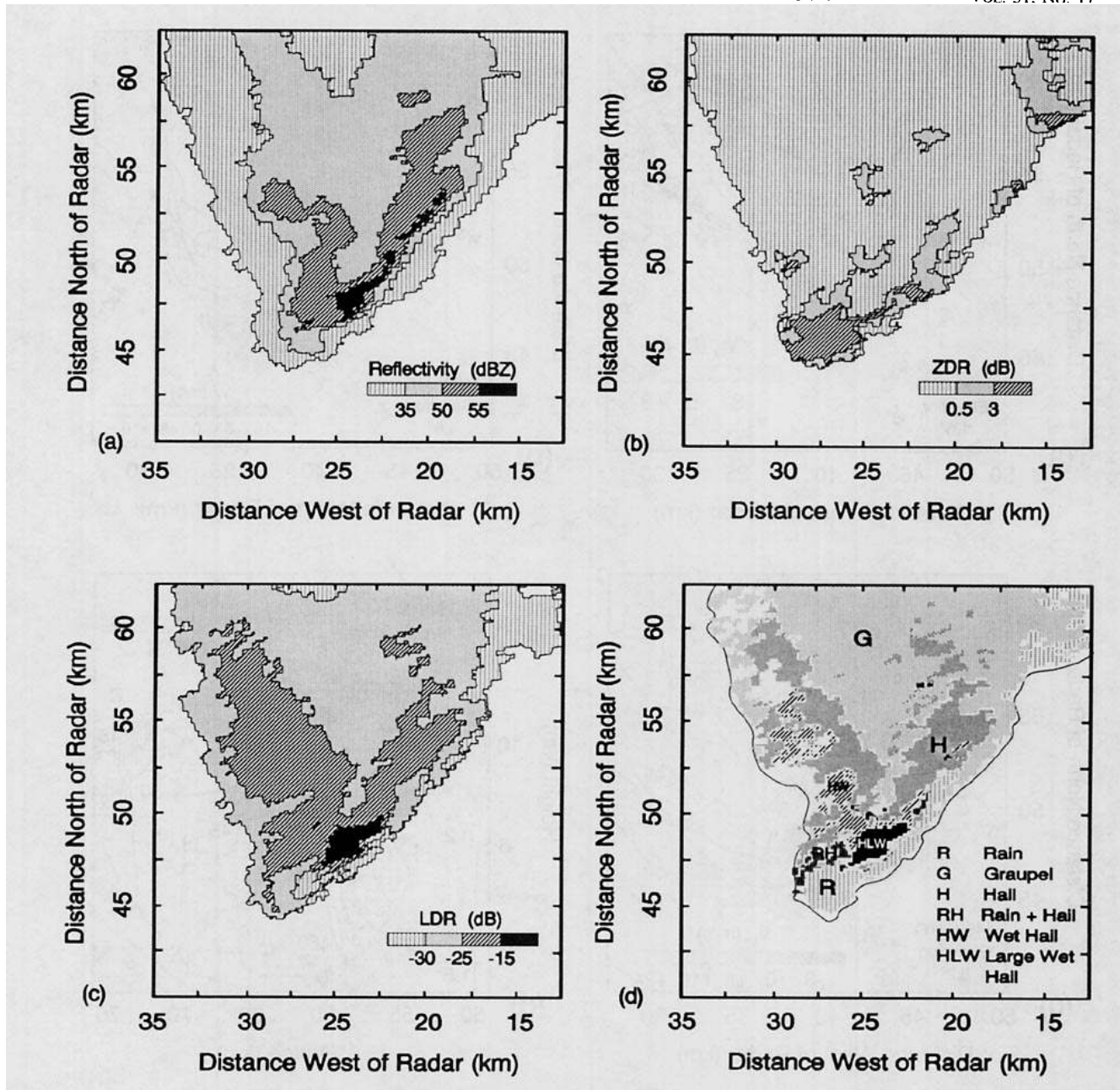
FIG. 8. Reflectivity Z_{HH} (a), differential reflectivity Z_{DR} (b), linear depolarization ratio LDR (c), and hydrometeor type (d) at 1450 UTC for 1.7° elevation, corresponding to about 1.8 km AGL at the storm's center.

nature. These are connected to the cellular structure, especially in the region of new updraft growth. Here several transient weak echo regions develop in sequence [discussed as discrete propagation by Foote (1985)]. This may indicate a multiple-branch updraft structure. These updraft regions sometimes show cyclonic rotation. According to the storm's unsteadiness, this rotation could not be detected permanently. Nevertheless, it might have been present in the echo-free zones. But the storm did not develop a large mesocyclone as is typical for supercells. One reason might be the relatively low cloud base. As can be concluded from Fig. 2, there is not much shear below cloud base. Therefore, we would expect that little horizontal vorticity will be tilted into the vertical, causing the updraft to rotate.

5. Microphysical interpretation of polarimetric radar parameters

The polarimetric signatures of precipitation are, among others, dependent on the size, shape, thermo-

dynamic phase, and tumbling behavior of the individual particles present in the observed volume. In this study, the following parameters are examined in more detail.

1) The differential reflectivity Z_{DR}, defined as

$$Z_{DR} \equiv 10 \log\left(\frac{Z_{HH}}{Z_{VV}}\right) \quad [\text{in dB}],$$

where Z_{HH} is the reflectivity factor for horizontally (H) or vertically (V) transmitted (first index) and received (second index) waves. In this study we are dealing with linear polarization exclusively.

2) The linear depolarization ratio LDR, where

$$\text{LDR} = 10 \log\left(\frac{Z_{HV}}{Z_{HH}}\right) \quad [\text{in dB}].$$

3) The specific differential phase K_{DP}

$$K_{DP} = \frac{2\pi}{k_0} \text{Re} \int [f_{HH}(D) - f_{VV}(D)]N(D)dD$$

$$[\text{in deg km}^{-1}],$$

where k_0 is the free-space propagation constant, f_{HH} and f_{VV} are the forward-scatter amplitudes at horizontal and vertical states, and $N(D)$ is the number density function of particles of size D.

4) The cross correlation ρ_{HV},

$$\rho_{HV} = \frac{\int S_{HH}(D)S_{VV}^*(D)N(D)dD}{\left[\int |S_{HH}(D)|^2N(D)dD \times \int |S_{VV}(D)|^2N(D)dD\right]^{1/2}},$$

in which S_{HH} and S_{VV} are the backscatter amplitudes at horizontal and vertical states, and the asterisk denotes complex conjugation.

It is not possible to derive all the microphysical information about particle distribution, phase, or type from these parameters alone. But a rough estimation of the prevailing particle type and size can be inferred, as has been shown in previous studies. Most of these studies have been done for 3-cm (X-band) or 10-cm (S-band) wavelength radar. Only a few deal with the 5-cm (C-band) wavelength, which is relevant for this paper. There are pronounced differences in backscattered signals for the different wavelengths as the precipitation particles may have dimensions comparable to the wavelength used (Mie scattering). Indeed, these differences have been successfully applied to hail detection in terms of the dual-frequency ratio (e.g., Bringi et al. 1986b).

The differential reflectivity Z_{DR} is a measure of the preferred orientation of nonspherical hydrometeors as well as of their mean axis ratio. Positive ($Z_{HH} > Z_{VV}$) or negative ($Z_{HH} < Z_{VV}$) values result from a preferred horizontal or vertical alignment of the larger axis of the particles. Positive values of Z_{DR} are caused by the oblate shape of raindrops whose major axes are highly oriented horizontally. Seliga and Bringi (1976) have demonstrated the use of differential reflectivity for rain detection. Good estimates of rainfall rate could be obtained by Z_{HH} and Z_{DR} measurements. Negative values of Z_{DR} can arise from large oblate hailstones with their major axis aligned around the vertical. Aydin et al. (1986) introduced a hail signal function H_{DR} for discriminating hail from rain. Two parameters were used: reflectivity and differential reflectivity. Based on distrometer data a separation line between rain and hail was defined. Here H_{DR} has proved to be a good indicator for hail, especially below the melting level (e.g., Bringi et al. 1986b).

As Z_{DR}, LDR is another measure of the preferred orientation of nonspherical hydrometeors. But it exhibits a different canting angle dependence as Z_{HV} is very low for horizontally or vertically oriented particles and increases to maximum values for canting angles of 45° (for axisymmetrical particles). Moreover, LDR shows a much more pronounced response to hydrometeor variability than Z_{DR} does. This specifically holds for ice particles. Therefore, LDR is especially useful for detecting graupel and hail above the melting level (e.g., Jameson and Johnson 1990). Furthermore, wet ice particles (melting or growing in the wet mode) can lead to an increase of LDR due to the enhanced refractive index of water as compared to pure ice. Bringi et al. (1986a,b) presented calculations of Z_{DR} and LDR for graupel and hail particle distributions and found good agreement with radar measurements for convective storms. The investigations reported on so far have been performed for 3-cm or 10-cm wavelengths. Calculations of polarimetric observables as well as radar measurements for 5 cm can be found in Bringi et al. (1991), Meischner (1990), Meischner et al. (1991), Vivekanandan et al. (1990), and Aydin et al. (1991).

The specific differential phase K_{DP} is, like Z_{DR}, dependent on particle shape. But, in a mixture of statistically isotropic and anisotropic particles (like tumbling hail or rain, respectively), it is affected by the anisotropic hydrometeors (rain) only (Balakrishnan and Zrnić 1990a). Therefore, KDP can be used to estimate the rain part in mixed phase precipitation.

The cross-correlation ρ_{HV} between co- and cross-polar echoes at zero time lag is also dependent on the characteristics of the hydrometeor distribution. This parameter is useful for characterizing the homogeneity of a mixture of hydrometeors (Balakrishnan and Zrnić 1990b). Large values of ρ_{HV}, close to unity, can be expected for a highly oriented medium with only little variation in the canting angle distribution of one type of particles (as for pure rain). On the other hand, a mixture of different types or shapes of particles

or irregularities in shape cause a decrease of ρ_{HV} values.

Since most of the radar data available for the storm considered provide us with Z_{HH}, Z_{DR}, and LDR, we use these parameters for investigating the time evolution of precipitation. For this purpose an interpretation scheme exclusively based on these polarimetric measurables is derived in the following. For selected RHI scans of time series additional parameters like KDP or ρ_{HV} are available.

The investigations reported on represent the database of polarimetric parameters available so far for the interpretation of the measurements obtained for the hailstorm studied here. Therefore, we are using these data as a general outline for a microphysical interpretation. On the other hand, the radar data are checked for characteristic structures in Z_{DR}–LDR space consistent with the theoretical considerations. Here Z_{HH} is not used for purposes of classification as it strongly depends on maximum particle size as well as particle concentration. The following scheme of interpretation was derived in a semiempirical manner. A summary is given in Table 1. Preferably, calculations performed for 5-cm wavelength were considered.

1) Small raindrops (diameters < 1 mm) are nearly spherical in shape or only slightly deformed, resembling oblate speroids, the major axis being horizontally oriented (Pruppacher and Klett 1978). Therefore, Z_{DR} is only slightly positive (<1 dB) and LDR is very low (< −35 dB). As small graupel or snow can produce the same Z_{DR}–LDR characteristic, we use the height of the melting level as deduced from an environmental sounding for discrimination.

2) With increasing size large raindrops (diameter > 1 mm) become more and more deformed, resembling oblate spheroids with flat bases (Pruppacher and Klett 1978). The drops are falling more or less aligned with their major axis horizontally. As compared to the small raindrops, larger positive values of Z_{DR} can be expected. For the purpose of this study, we choose Z_{DR} = +1 dB as a boundary for distinguishing small rain from large rain hydrometeors. Scattering calculations

for raindrop distributions have been presented by Meischner (1990) and Bringi et al. (1991). The results show that Z_{DR} = 1 dB corresponds to a median volume diameter of the drops of about 1.25 mm for an exponential size distribution. In the small raindrop range LDR is less that about −35 dB. With increasing drop size and oblateness LDR increases too as the drops are assumed to be canted by a few degrees relative to the horizontal. An upper limit of −25 dB has been assumed for LDR of rain, as higher values could also be caused by mixtures of hail and rain.

3) Snow or small, dry graupel is characterized by Z_{DR} around 0 dB (for discrimination from rain an upper boundary of +1 dB is chosen) and very low LDR. This is caused by tumbling motions of snowflakes or riming graupel, which might have conical shapes. Prolate shapes can also cause slightly negative Z_{DR} values. Bringi et al. (1986a) have shown computations for conical graupel as well as radar and aircraft measurements.

4) If the graupel particles are growing in the wet mode or are melting, they become covered by a layer of liquid water or may soak the liquid into their interior. For such particles LDR becomes higher than for dry graupel. LDR may also increase with increasing graupel size as these particles intensify tumbling. The transition to small hail sizes is also included here. Again, calculations of the polarimetric parameters of melting graupel are presented in Bringi et al. (1986a).

5) Even though hailstones may be quite irregularly shaped, they often can be approximated by oblate spheroids. Hailstone shape factors (ratio of minimum to maximum dimension) show a generally decreasing trend with increasing maximum dimension (Knight 1986). During free fall the stones tumble, rotate, or gyrate, causing Z_{DR} to be relatively small (−1 dB < Z_{DR} < +1 dB). According to the preferred orientation, Z_{DR} is positive or negative. As hailstones have dimensions comparable to the wavelength used (5 cm), resonance effects in the Mie scattering regime can even reverse this general trend. Scattering calculations

TABLE 1. Empirical interpretation scheme used for hydrometeor discrimination in Z_{DR}-LDR space. H_{MELT} is the height of the melting level. Z_{DR} and LDR in decibels.

Hydrometeor type	Symbol	Parameter range		
Small raindrops	r	$Z_{DR} < +1$	LDR < −35	$H \leq H_{MELT}$
Large raindrops	R	$Z_{DR} \geq +1$	LDR < −25	
Graupel (dry, small), snow	S	$Z_{DR} \leq +1$	LDR < −35	$H > H_{MELT}$
Graupel (wet, melting, small), Graupel (dry, large), hail (dry, small)	G	$-1 \leq Z_{DR} < +1$	$-35 < LDR \leq -25$	
Hail (dry)	H	$-1 \leq Z_{DR} \leq +1$	$-25 < LDR \leq -20$	
Hail (wet)	HW	$-1 < Z_{DR} \leq +1$	$-20 < LDR \leq -15$	
Large wet hail (spongy or water shell)	HLW	$Z_{DR} \leq +1$	LDR > −15	
Rain + small hail (wet)	RH	$Z_{DR} \geq +1$	$-25 < LDR \leq -20$	
Rain + large hail (wet)	RLH	$Z_{DR} \geq +1$	LDR > −20	

shown by Meischner (1990) or Aydin et al. (1991) demonstrate these effects. As compared to the graupel particles, LDR increases further if dry or even wet hailstones are present. The largest values can be expected for particle distributions containing a relatively high concentration of large particles. As a general guideline for the hydrometeor classification, we have used calculations based on (exponential) size distributions of the particles. The results of Aydin et al. (1991) have shown that LDR is a much better indicator of hail wetness than Z_{DR} can be. Therefore, in this study wet hail is discriminated from dry hail by an LDR criterion (see Table 1) allowing Z_{DR} to vary between -1 and $+1$ dB in both cases. Aydin et al. (1991) also show that appreciable deviations from these results can be expected for monodispersed hail due to resonance effects. For instance, Z_{DR} varies considerably with hail size. Negative values well below -1 dB and positive values well above $+1$ dB both are possible. These deviations are even more pronounced as the hail melts. Wet or melting hail can cause large negative values for equivolume spherical diameters of around 2.5 cm and large positive values for diameters around 1 cm. Meischner et al. (1991) obtained a maximum Z_{DR} of 9 dB for a single melting ice core surrounded by a water shell of initially 7.3 mm in diameter. In the present classification scheme negative Z_{DR} is attributed to the large and wet hail category, whereas the large positive values are assumed to occur in mixed phase precipitation (melting hail mixed with rain).

6) Mixed phase precipitation is assumed to be represented by transitional values from the dry ice particles to the rain medium. As graupel particles will probably melt relatively quickly into raindrops, we consider only rain–hail mixtures. For simplicity, we assume the mixture to be characterized by Z_{DR} values in excess of $+1$ dB. LDR is used as a measure of hail size in a mixture.

It should be emphasized that the interpretation of the polarimetric parameters presented here does not cover all of the possible hydrometeor types in a convective storm. For instance, melting snow, which can produce the well-known brightband effects (enhancing the parameter values), is not taken into account. In this case the two-parameter scheme will show ambiguities as the expected Z_{DR} and LDR values would also result from hail or mixed phase precipitation. But, as brightband phenomena appear only rarely in strong convective cells, they do not affect the interpretation to a large extent, at least for the storm discussed in this paper.

The data presented here have not been corrected for attenuation effects. Attenuation and differential attenuation can be expected to be important for significant rain paths of the radar beam. The hydrometeor classification scheme does consider this by ignoring those values located to the rear of high Z_{DR} regions. More details will be given in section 8. But measurements of

the hail growth zones, which are the main focus in this paper, are not affected severely by attenuation. This is due to the lack of appreciable amounts of interlaying precipitation on the path to the radar.

The classification given above should be looked upon as a qualitative tool for interpretation of the hydrometeor types in a hailstorm. Due to the lack of in situ verification as well as more complete scattering calculations, there is still a high degree of subjectivity in the definition of the particle categories and the separating boundaries between them. The inclusion of the additional polarimetric parameters discussed above does refine the general picture described here. We will demonstrate this for some selected radar scans in the following.

6. Polarimetric and microphysical characteristics of the storm

We discuss now the polarimetric characteristics of the storm and give a microphysical interpretation in terms of particle types. The evolution of the storm in connection with the flow structure presented above allows some conclusions about the relevant microphysical processes.

Figures 8 through 10 show Z_{HH}, Z_{DR}, LDR, and the inferred hydrometeor type for different elevations. Concerning Z_{DR}, two dominant features can be noted in the high-reflectivity region at the lowest elevation: (a) a zone of high Z_{DR} values (up to about 6 dB) at the leading edge of the storm and (b) the low Z_{DR} values ($< +0.5$ dB) associated with the reflectivity maximum (>60 dBZ). In region (a) the LDR values are relatively low, whereas very high LDR values (up to -11 dB) are correlated with the high reflectivity and the low Z_{DR} values in region (b). The microphysical interpretation of these data is shown in Fig. 8d. A core of large and wet hail is surrounded by other types of hydrometeors. Pure rain can be seen at the southeastern flank of the storm. The main hail shaft coincides with the storm's maximum downdraft and west to northwesterly relative winds. The rain and mixed phase precipitation at the south and southwestern edge of the storm are falling through the updraft air, which is entering the precipitation field from the southeast. Thereby it is suggested that the particles in this region originate from higher levels rather than from the main precipitation shaft.

At midlevels (Fig. 9) the region of high Z_{DR} values is still present but has decreased considerably in its horizontal extent. It is located at the southeastern flank of the storm's high-reflectivity region. This corresponds to the northwestern side of the WER as well as to the growing cell region at the storm's southwesterly flank. In these zones LDR has relatively low values (-35 to -30 dB) as compared to the other regions of the storm (maximum of about -15 dB in the high-reflectivity region). Rain and rain mixed with small hail are ana-
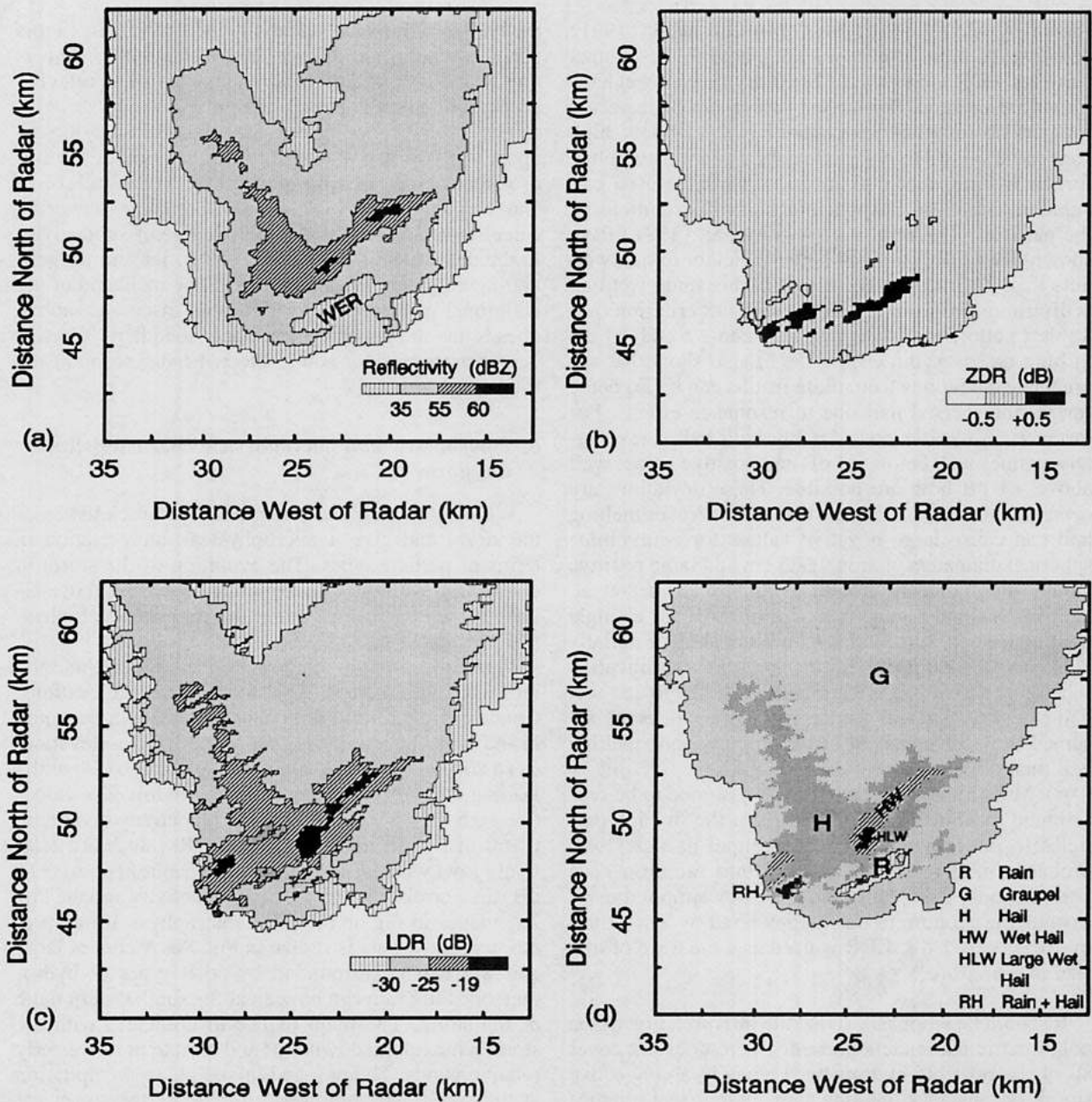
FIG. 9. Reflectivity Z_{HH} (a), differential reflectivity Z_{DR} (b), linear depolarization ratio LDR (c), and hydrometeor type (d) at 1450 UTC for 4.1° elevation, corresponding to about 4.0 km AGL at the storm's center. WER indicates the weak echo region.

lyzed for the high-Z_{DR} region. Hail is inferred in the V-like pattern with an embedded core of wet and even large wet hail. This pattern is surrounded by a large region of graupel. As in the lower levels, the flow in the new cells is from the south to southeast and is generally embedded in the updraft zone, whereas the rain at the edge of the main storm core is in the transitional zone from downdraft to updraft in a horizontally convergent wind field.

At high levels (Fig. 10) Z_{DR} is scattered around 0 dB, showing no coherent structure. LDR is positively correlated with the reflectivity. These patterns are indicative of a core of hail to the south and an anvil region of graupel to the north.

The vertical structure of the polarimetric parameters is shown in Fig. 11. The scan has been taken about 10 min prior to the PPI scans used for constructing the horizontal sections. The reflectivity structure clearly
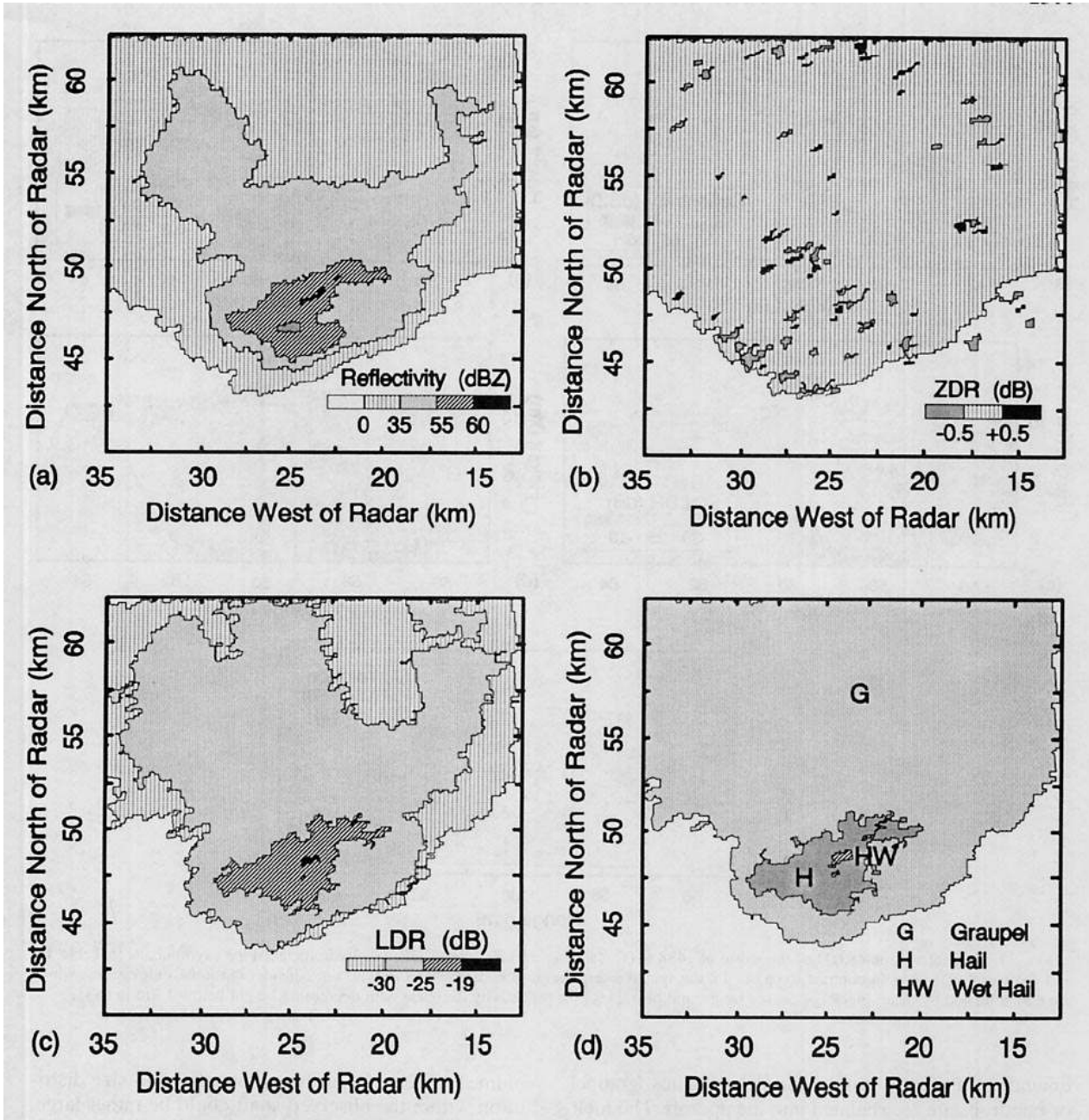
FIG. 10. Reflectivity Z_{HH} (a), differential reflectivity Z_{DR} (b), linear depolarization ratio LDR (c), and hydrometeor type (d) at 1450 UTC for 7.7° elevation, corresponding to about 7.5 km AGL at the storm's center.

shows the region of overhanging echo extending from a height of 4 km at a distance of 55 km to a height of 9 km at a range of 60 km, corresponding to cells 6, 7, and 8. Another zone of high-reflectivity values marks a decaying cell centered at a range of 58 km near the ground. A weak echo region (WER) is separating these maxima. The decrease in reflectivity at very low heights is caused by a beam blockage effect from trees and hills in the vicinity of the radar.

Positive values of differential reflectivity correlated with low LDR can be seen in the lower regions of the reflectivity overhang up to 3 km AGL, in the WER and at the edge of the main precipitation shaft. These zones are analyzed as rain regions (Fig. 11d). The Z_{DR} values around 0 dB are prevailing in all other regions. Closer examination reveals a positive Z_{DR} column with the 0.5-dB contour extending to 5 km. The column location appears to be at the intersection of the main updraft and
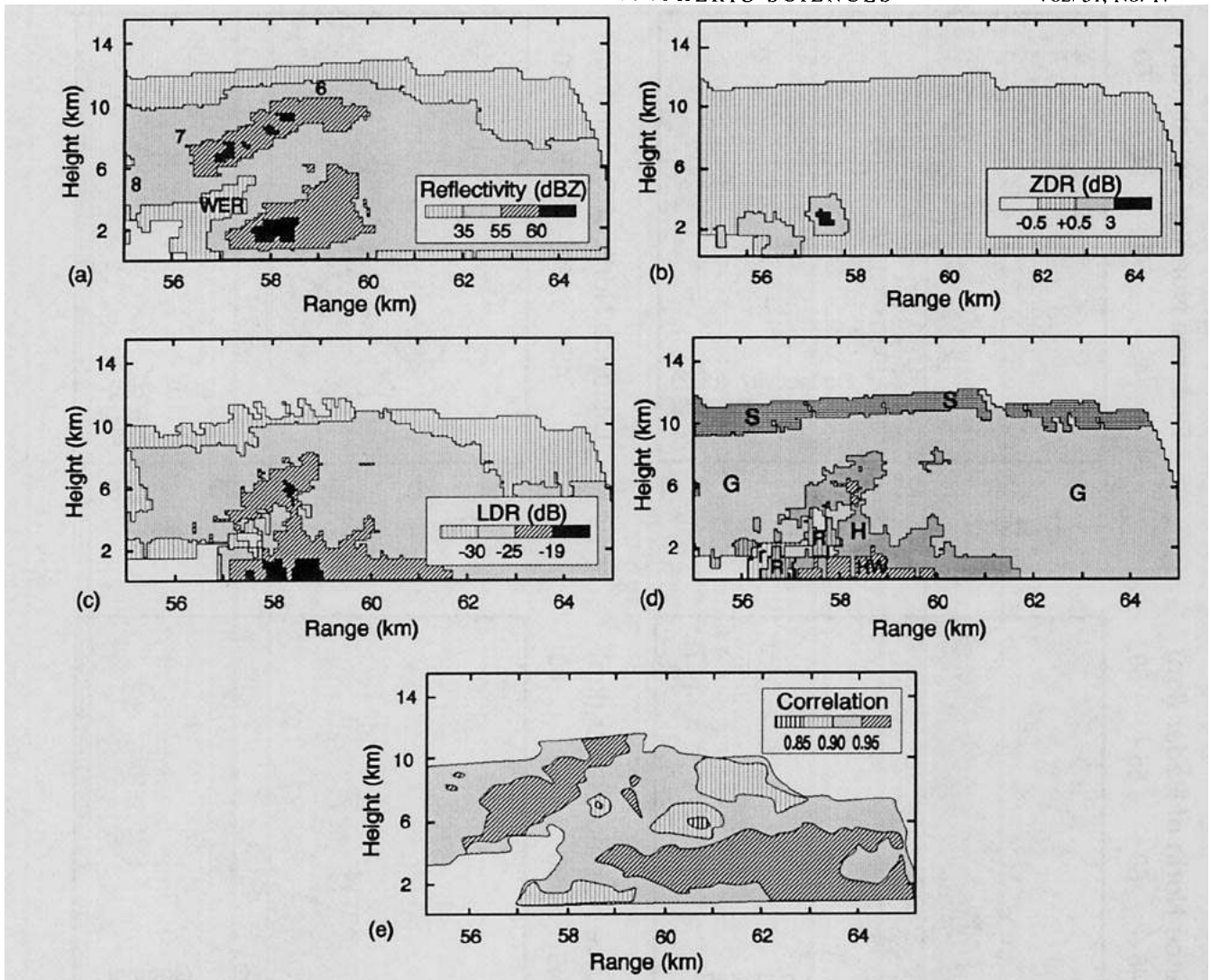
FIG. 11. Vertical section (RHI) of the storm at 1438 UTC: (a) Z_{HH}, (b) Z_{DR}, (c) LDR, (d) hydrometeor type (symbols as in Table 1), and (e) correlation ρ_{HV}. In contrast to (a)–(d), the spatial interpolation scheme used in (e) did not consider the lowest elevations, which are contaminated by beam blockage caused by ground obstacles [see reflectivity decrease with decreasing height below 1 km in (a)].

downdraft. Possibly small melting hailstones, graupel, or raindrops are recirculated into the updraft. The melting ice particles appear oblate in shape like a raindrop with an inner ice core.

The combination of high Z_{HH} and $Z_{DR} \approx 0$ dB within the main precipitation shaft indicates hail. The K_{DP} data show values close to zero in this region, suggesting precipitation is dominated by hail with negligible rainfall rate. In this region high LDR (> -19 dB) and low ρ_{HV} are found. This combination of high Z_{HH} with Z_{DR} and K_{DP} around 0, high LDR, and low ρ_{HV} can be compared with the scattering model calculations of Aydin and Giridhar (1991), based on the hail melting model of Rasmussen and Heymsfield (1987a,b) and the English and Cheng (1984) exponential hailstone size distribution. Such a comparison indicates that the median

volume diameter D_0 of the exponential hail size distribution within the observed shaft could be rather large, in the range 15–25 mm.

Another region of enhanced LDR (-23 to -17 dB) can be found aloft above the WER where Z_{DR} is slightly negative (-0.5 to 0 dB) and ρ_{HV} is high (up to 0.98 at a range of 56.8 km and height 6.5 km). This is a region of hail growth (graupel and small hailstones) dominated by one kind of particle type rather than a mixture of different particle types. Such a mixture as characterized by lower values of ρ_{HV} can be found within the main precipitation shaft.

The two-way differential propagation phase Φ_{DP}, from which K_{DP} is derived, was found to be very small ($\sim 10°$), even through the main precipitation shaft. The maximum K_{DP} was around $1°$ km^{-1} at range 62 km and

height 1.2 km, that is, NW of the main precipitation core. It may be inferred that the maximum rainfall rate at this time was no more than around 20 mm h^{-1}, indicating that the storm was an efficient hail producer.

In the new cells LDR varies around −30 dB, increasing with increasing reflectivity with values up to −17 dB in the main overhang. Even higher values of LDR (−14 dB) can be found in the main precipitation shaft below 3-km height. This is interpreted as a core of hail embedded in the graupel region of a new cell and a decaying hail cell releasing melting hail to the ground.

The horizontal and vertical structure of the storm discussed in this section again is representing a snapshot in the life cycle of the storm. But many features of the flow field as well as of the polarimetric characteristic are quasi-steady. Among those features are the anticyclonical rotation of the updraft–downdraft pair at the southwestern side and the presence of raindrops at the edge of the reflectivity core and in the new cells to the southwest. The more or less transient features of the storm are associated with its cellular structure. But, because of their transient nature, they allow tracking evolutionary processes of the particles contained in them. This will be shown in the following section.

7. Discussion of particle growth

The microphysical processes determining the growth of precipitation particles will be discussed in this section as far as they can be inferred from the polarimetric measurements. Among these processes are the initiation of precipitation (liquid or ice processes), the subsequent growth of graupel and hail, shedding of drops from hail, melting of ice particles, and recirculation processes of raindrops.

For deducing these characteristics of particle growth, it is essential to assess the conditions under which this growth takes place. For this purpose we make use of a simple parcel model of a one-dimensional vertical ascent of cloudy air. Using the environmental sounding for obtaining the initial conditions at cloud base, the vertical equation of motion and the thermodynamic equation are solved for updraft velocity and cloud temperature. Droplet and ice particle spectra are computed by considering microphysical processes like coalescence, freezing, and riming. Details of the model are described in Höller (1983, 1986). Figure 12 shows vertical profiles of temperature and updraft velocity. More details of the model results will be given in the following discussion.

The evolution of precipitation with time can be inferred from a series of RHI scans through the storm's core, as shown in Fig. 13. Here we concentrate on the growth of the large hailstones finally falling out in the high reflectivity zone adjacent to the weak echo region. For this purpose we follow the evolution of cell 6.

A crucial point for precipitation development is the initialization phase. Principally, liquid and ice phase
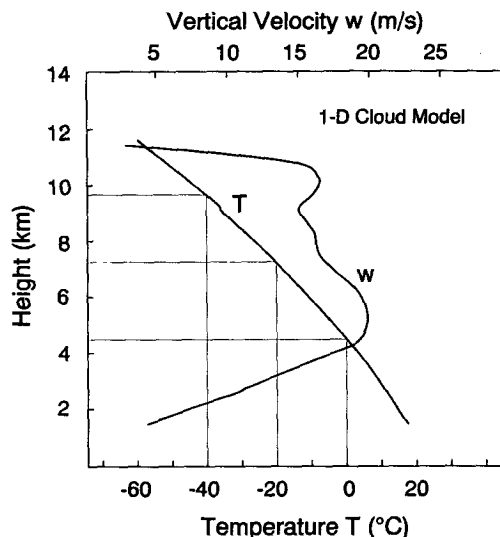

FIG. 12. Vertical profiles of cloud temperature and updraft velocity as obtained from one-dimensional cloud model computations. Heights refer to sea level.

processes must be considered. Collision and coalescence of water drops might lead to rain formation without the ice phase being involved. On the other hand, ice particles grown by nucleation can rime in the presence of small cloud droplets and finally reach graupel or even hail sizes. The subsequent melting of ice can produce raindrops.

Cell 6 developed between 1425 and 1430 UTC from a very weak first echo at 4 to 6 km AGL to a 40-dBZ core extending from 4 to 8 km AGL at the southernmost edge of the storm. The initial stages of the newly grown cells with reflectivities up to about 20 dBZ typically have LDR values not exceeding −30 to −25 dB while Z_{DR} is approximately 0 dB. In this stage of development small raindrops (drizzle) cannot be discriminated from snow or small graupel particles by radar measurements. Both types of particles would be consistent with these measurements. If rain were present, the polarimetric values would indicate drops with diameters less than 1 mm. This also holds for the subsequent development of precipitation. LDR increases (up to −25 to −23 dB) with increasing reflectivity (30 to 40 dBZ) but Z_{DR} does not change, basically fluctuating around 0 dB and thus indicating the presence of graupel. These observations are still consistent with two possible scenarios: (i) raindrops grow by coalescence to drizzle drop sizes and freeze, their diameters in the supercooled stage not exceeding 1 mm, or (ii) graupel form by riming of ice crystals initialized by vapor deposition. Precipitation particles grown in either of these two paths then grow further into larger graupel or hail by coalescence with water drops.

For assessing which of the two possible scenarios of precipitation initialization is more probable to occur
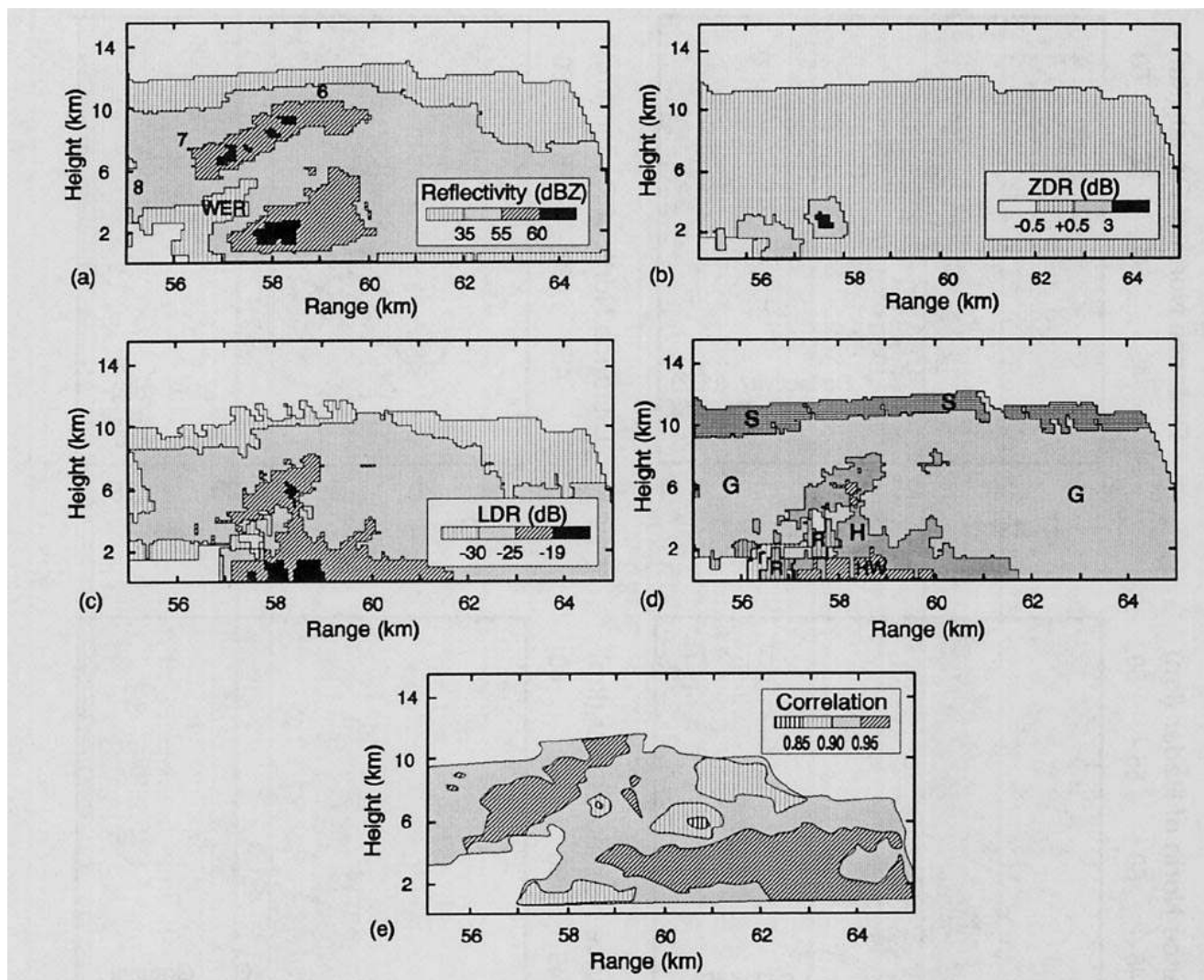
FIG. 13. Sequence of RHI scans through the storm's core: (a) 1431 UTC at 323°, (b) 1432 UTC at 324°, (c) 1436 UTC at 326°, (d) 1438 UTC at 328°, (e) 1445 UTC at 330°, and (f) 1448 UTC at 332°.

under the given cloud environment, we inspect the temperature range in which these processes are operating. From Fig. 12, we note that the in-cloud melting level (0°C) is at 4.3 km MSL (3.7 km AGL), the −10°C level at 6 km MSL (5.4 km AGL), the −20°C level at 7.2 km MSL (6.6 km AGL), and the −40°C level at 9.7 km MSL (9.1 km AGL). From the development of a first echo from cell 6, but moreover from other cells that are covered by radar measurements just after the formation of precipitation, we can roughly estimate the level of precipitation formation to be located at 5 km AGL (or 5.6 km MSL). Temperatures here are as low as −10°C. Following the results of Pitter and Pruppacher (1973), the median freezing temperatures of drops of 1 mm in diameter are ranging from −28°C to −15°C, depending of the purity of the water. Thus, the coalescence–freezing hypothesis does not seem to be consistent with these data, suggesting that the subli-

mation–riming process of ice crystals is responsible for precipitation formation.

Some further indirect evidence for an ice phase initialization is given by the occurence of big drops in other parts of the storm. Large supercooled raindrops never did appear in the center of the new cells, a fact which could be explained by freezing of these drops well before reaching larger sizes as discussed above. Since such a freezing process had to be finished at around 5-km height, large drops, characterized by high Z_{DR} values, should not appear at these heights or even higher up in the storm. In contrast, large drops were detected up to 6 km AGL, but in the main updraft region only where we expect temperatures down to −15°C. These drops, which should exceed 1 mm in diameter, were observed at heights well above the level of echo formation in the new cells. These polarimetric features suggest that large supercooled drops associated

with Z_{DR} values larger than 1 dB did not freeze until reaching the $-15°C$ level within the main updraft. Therefore, it seems unlikely that smaller drops, which might have been formed in the new growing cells, would freeze at even higher temperatures ($-10°C$) at lower heights because the freezing temperatures of drops generally increase with increasing drop size. If it is assumed that the spectra of ice-forming nuclei are the same within the main updraft and the newly growing cells, it must be concluded that cloud droplet freezing was not the precipitation initialization process.

The question of the origin of large drops still remains to be explained. Consistent with the Doppler data (Fig. 7), the main source of large drops in the weak echo region is the melting of graupel formed in the new growing cells, falling below the melting level, and then being recirculated in regions of higher updraft speeds. This process is clearly recognizable in Fig. 13b for cell 6 as well as in the schematic diagram of Fig. 14. From the young cells close to the radar (cell 6 in Figs. 13a,b and region G in Fig. 14b), graupel are falling down to the melting level at about 4 km AGL. The drops in region R_1 of Fig. 14 are advected horizontally toward the storm's center (dashed arrows, Fig. 14b). The larger drops falling in weak updraft continue to fall downward (lower dashed arrow), while some of the drops may penetrate into regions with higher updraft speeds where they can be lifted to higher altitudes in the main updraft zone (upper dashed arrow). Here they can be detected as part of the forward flank overhang as well as in the weak echo region (W in Fig. 14b). These processes are characteristic of the rear flank (to the southwest) of the storm's updraft zone.

In the main updraft region the graupel particles are not able to penetrate downward as far as they did on the southwestern flank. At 1432 UTC the tip of the forward flank overhang is not a very productive source of large drops, even though drops are present in the adjacent weak echo region. These drops may have originated from graupel melting in the main updraft where the freezing level is expected to be located at a somewhat higher altitude than in the surrounding air of the feeder cells, which is probably influenced by mixing with cooler environmental air. Since the main updraft region might be unmixed, very high liquid water content (LWC) can be expected, especially in the weak echo region which is not influenced by depletion of cloud water by accretion. Cloud model computations for the adiabatic case (no mixing with environmental air) result in water content of 5 g m^{-3} at the freezing level and 5.5 g m^{-3} at the $-20°C$ level. Relatively warm temperatures and high liquid water content represent conditions most favorable for wet growth of hailstones. Following the computations of Bailey and Macklin (1968), hail of all sizes is expected to grow in the wet mode at nearly all temperatures from the melting level up to the homogeneous freezing level at about $-40°C$, located at about 10 km AGL for the adiabatic case. Precipitation particles falling through the updraft under these conditions occasionally produce Z_{DR} values in excess of 6 dB, indicative of large drops having an ice core inside.

Higher up in the main updraft region mostly graupel or hail particles are present (region H in Fig. 14). This has already been demonstrated by Fig. 11 in the previous section. Cell 6 is shown here reaching cloud top and developing a reflectivity core in excess of 60 dBZ at a height of 8 to 9 km (Figs. 11a, 13d). This core is nonhomogeneous, as far as its microphysical composition is concerned. LDR increases steadily from the outermost to the innermost (adjacent to the WER) parts (Fig. 11c). This can be interpreted as a transition from graupel to hail particles. The growth of large hail is favored in the vicinity of the WER. Close to the center of the WER, as well as to the same extent inside the WER, hail grows in the wet mode (region HW in Fig. 14a). Obviously, large hailstones (in low concentration because of the low reflectivity) are growing in a region of high liquid water content, whereas graupel or small hail (in higher concentration) is present in the areas surrounding the main updraft. The orientation of the WER in the vertical is indicative of the inclination of the updraft in the vertical. Therefore, hail embryos can be advected horizontally across the updraft into the WER where further growth into large hail can occur.

A decaying older cell is also seen (Fig. 11 at 56- to 61-km range) releasing its precipitation to the ground. Melting hail is probably the dominant type of precipitation here (WH in Fig. 14) based on the relatively high values of LDR and Z_{DR} around 0 dB. An exception is the zone located closest to the radar at 56 to 57 km. It is likely composed of rain (R_2 in Fig. 14) as indicated by low LDR and high Z_{DR} values. Such a microphysical structure of the precipitation shaft may be explained by a size sorting in the horizontal wind field associated with the downdraft. Because of its higher terminal velocity, hailstone trajectories (right dotted arrow in Fig. 14b) are oriented more vertically than those of raindrops (left dotted arrow Fig. 14b). The rain might have originated from melting of graupel or smaller hail. This feature is more or less a persistent one and is characteristic for the structure of the main precipitation shaft at low levels. In combination with the raindrops aloft, which have their origin in recirculation processes, these drops often form a coherent zone ($R_1 + R_2$ in Fig. 14) of large drops filling the WER at least in its lower parts. At higher levels the drops may be supercooled. With still increasing height this zone is bounded by a region of wet growing hail. From Figs. 11 and 13, it is suggested that these hailstones originate from those growing in cells 6, 7, and 8 aloft and subsequently crossing the main updraft. But it is also possible that at least some of the wet hail arises from the freezing of supercooled raindrops.

The release of precipitation from cells 6, 7, and 8 is shown in Fig. 13e at 1445 UTC. Cell 6 is already in its
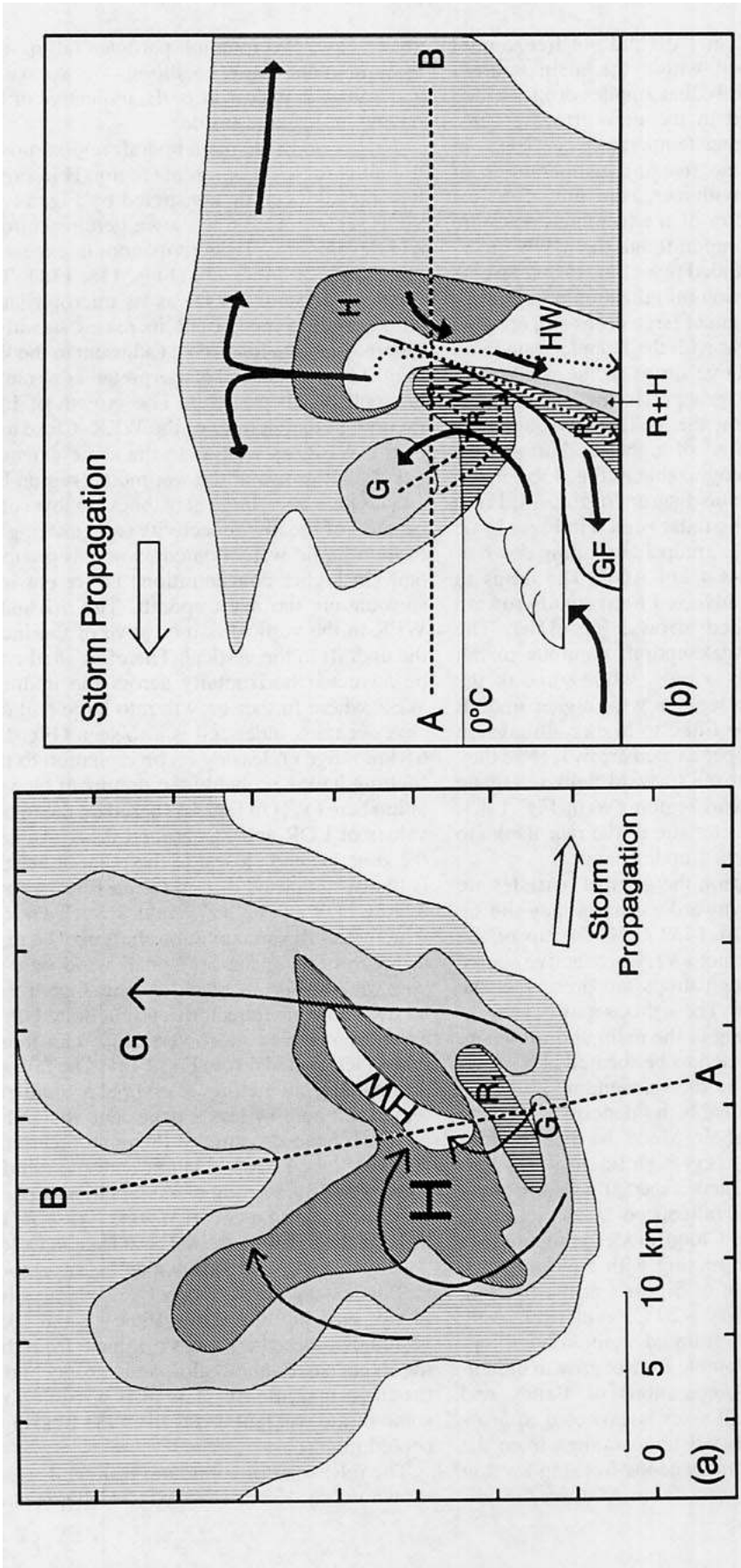
FIG. 14. Schematic diagram of the main dynamical and microphysical features of the hailstorm. Panel (a) shows a typical midlevel (about 5-km height) cross section. The arrows indicate horizontal streamlines. Panel (b) shows a typical vertical cross section along **A–B**. Solid arrows indicate streamlines; dashed and dotted arrows represent particle trajectories. Rain is found in region R_1, originating from melting of graupel from the newly grown cell (**G**). Some of these raindrops do recirculate into the weak echo region (**W**), where they are carried up to height well above the freezing level. Rain in region R_2 can have its origin either from drops passing through R_1 at relatively low trajectories or from melting or shedding hailstones in the main downdraft. The horizontal component of the velocity field causes a size sorting of rain, mixed particles, and wet hailstones (**HW**) on their way to the ground. The position of the gust front is marked by GF.

decaying stage; cell 7 is more or less in a mature stage, reaching maximum height but already accompanied by the fallout of hail to the ground. Cell 8 is still growing, the WER being associated with it at this time. The hail that grew in cells 6 and 7 is now hitting the ground at a range of about 55 km, close to the forward edge of the storm (see Fig. 15 for ground truth). This hail is only preceded by a relatively narrow rain region associated with the high Z_{DR} region (as in Figs. 8b or 11b). At longer ranges hail becomes more and more mixed with rain, again reflecting a size sorting of hydrometeors by the wind field as the smaller particles released from cell 6 melt before reaching the ground.

At 1448 UTC (Fig. 13f) cell 8 has intensified further in its forward-flank overhanging part. The WER is relatively narrow and extends up to about 7 km AGL. A column of wet hail extends from 7 km down to the ground.

8. Verification of the microphysical interpretation

Some interpretation of the polarimetric data presented in the previous sections can be substantiated by observations of hail damage at the ground. The data were provided by hail insurance companies, and these observations form a relatively dense ground-based network. Figure 15 shows the hailswath extending about 120 km in length from west to east with a width varying between 5 and 14 km. Contours with different degree of hail damage are shown. The particle categories (Table 1) containing hail are grouped as follows: (G) large graupel or small hail (as G in Table 1), (SH) small hail mixed with rain (as RH in Table 1), (IH) hail of intermediate size (dry and wet, H + HW in Table 1), and (LH) large hail mixed with rain as well as wet and spongy large hail (RLH + HLW from Table 1). A low-level PPI at 0.5° elevation was used to construct the track of the radar-derived hailswath. The contours have been advected horizontally with the speed of the mean storm motion for a period of time according to the time increment between two consecutive scans. The larger hail categories are preferably plotted in the case of coincidence of two different hydrometeor types at one grid point (caused by the transformation of the radar data to a Cartesian grid).

As a PPI scan has been used for the construction of the hailswath, the data do not originate from a constant level. At the storm's closest distance from the radar site this level is about 0.5 km AGL and at a range of 100 km about 1.5 km AGL. Therefore, it must be assumed that the graupel and small hail particles will melt, at least partly, on their way down to the ground. The hail signature shown will overestimate the amount of hail at the ground. Nevertheless, the larger hail particles will have a good chance to reach the ground without such an appreciable degree of melting due to their large ice mass as well as their large terminal velocities. Propagation effects, manifested by a Z_{DR} decrease and an

LDR increase with range, are another source for overestimating the amount of hail in or behind rain regions. They have been considered so far by ignoring those data points with Z_{DR} smaller than -2 dB that are located behind rain regions with Z_{DR} larger than 3 dB. Three-body scattering effects, as described by Zrnić (1987), represent another source of error in hydrometeor discrimination. These so-called hail spikes could be observed frequently as radially aligned protrusions behind high-reflectivity cores. They are not confined to reflectivity but are present in Z_{DR}, LDR, or Doppler velocity. A simple correction was done by ignoring very high LDR values (> -20 dB) associated with relatively low reflectivity (<35 dBZ) behind a high-reflectivity (>50 dBZ) core.

From Fig. 15 we note generally good agreement of the damaged area and those categories including hail except for the small hail and large graupel, which probably melt on their way down to the ground without causing damage there. At the southern edge of the hailswath we can find a narrow zone of hail reports that are not supported by the radar observations. This difference may be attributed to the horizontal advection of hydrometeors by the northwesterly winds of the downdraft air spreading out behind the storm's gust front below the low-level radar PPI. The hail reports at the easternmost parts of the hailswath deviate considerably from the radar-based hail signal and cannot be explained by horizontal transport. The exact time of the hailfall was not recorded by the insurance companies. Therefore, it is possible that these damages were caused by another hailstorm hitting the area later after midnight in connection with a squall line passage. This event was not covered completely by radar observations. There is no indication, however, that the rest of the ground-based data have been influenced by hail not originating from the storm discussed in this paper.

The finescale structure of the hailswath shows some interesting details. The hailfall is not a strictly constant phenomenon, but is rather of an oscillatory nature. The hail reports clearly show distinct centers with a high percentage ($>80\%$) of crop damage. Such areas of increased hail intensity within a hailswath have been termed hailstreaks (Changnon 1970) and have been identified as the tracks of individual hailshafts. As the ground-based data represent hail reports exclusively, they do not give any evidence for the hailstreaks to form distinct areas of hailfall separated by rain-only regions, as found by Changnon for most of the hailstorms investigated. Such a pattern cannot be excluded here even though it is suggested by the radar data that the hailswath is made up by a single hailstreak of varying intensity. The centers of the hailfall maxima are spaced 20 to 30 km in the direction of storm propagation. This corresponds to a period of 30 to 45 min. This type of long-amplitude oscillation is superimposed on the more short-term period of new cell formation and generally comprises several cells. A similar behavior
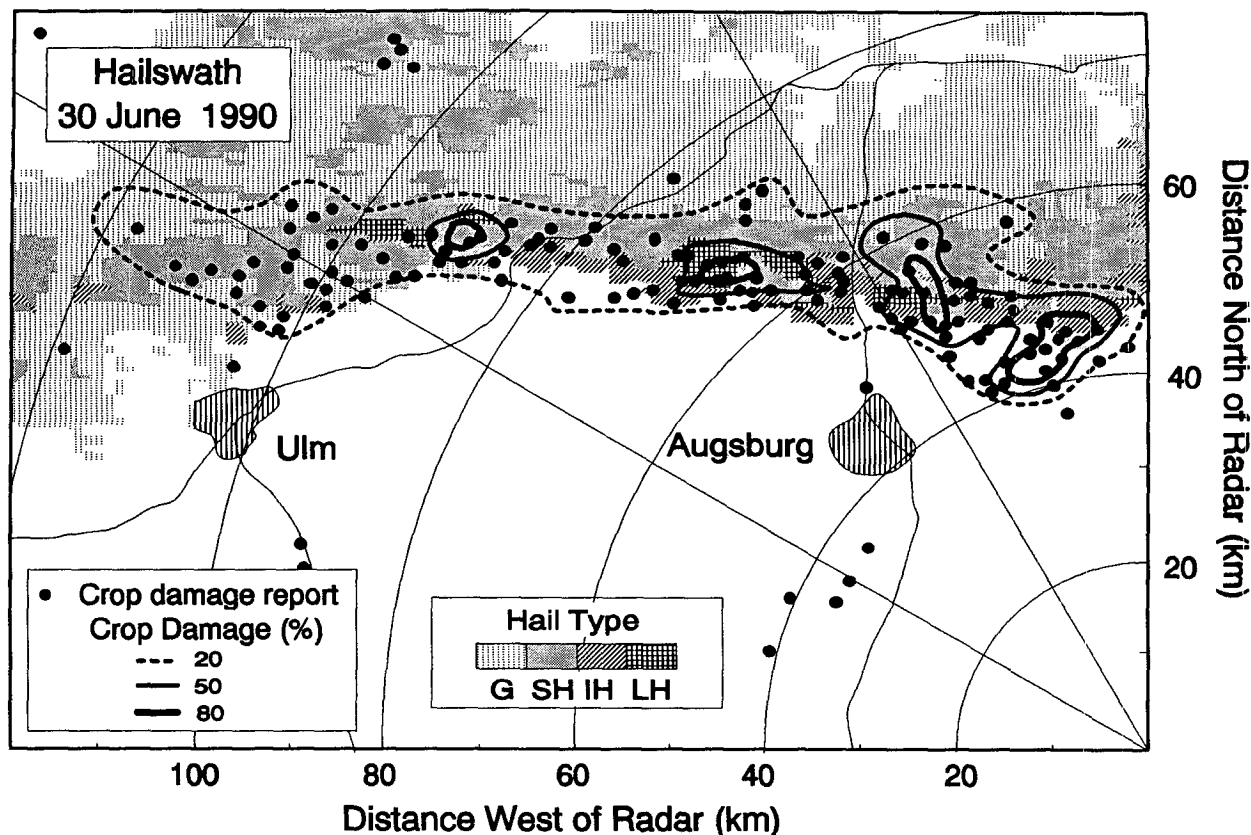
FIG. 15. Hailswath constructed from data of hail damage at the ground (kindly provided from hail insurance companies) and hydrometeor-type classification defined in this paper. The location and the degree of crop damage are shown. The hydrometeor categories are summarized according to hail size: (G) large graupel or small hail (as G in Table 1), (SH) small hail mixed with rain (as RH in Table 1), (IH) hail of intermediate size (dry and wet, H + HW in Table 1), and (LH) large hail mixed with rain as well as wet and spongy large hail (RLH + HLW from Table 1). The position of the radar is at the origin of the coordinate system.

of storm variability was found by Fovell and Ogura (1989) in their numerical study of storm development. With increasing low-level shear the simple oscillations of a repetitive multicellular state changed to more complex oscillations with secondary cells more comparable to the weak evolution or quasi-steady-state classification of Foote and Frank (1983).

It is highly instructive to note that the large amplitude oscillatory pattern of the hailswath coincides very well with the radar-derived large hail categories, which validates the multiparameter hail signature defined in this paper. Large hail is characterized by very high LDR values. The main burst of hail between 1420 and 1435 UTC was preceded by an enlarged area of over-hanging echo mass accompanied by recirculations of big drops, as shown in Fig. 16. The growing wet hail (HW) can be seen from heights 5 to 8 km. At lower levels this region is accompanied by rain extending from the overhanging echo below the melting level to the ground as well as in a column up to about 6 km. Here it is associated with reflectivity values up to 50 dBZ, thus indicating that a fairly high amount of liquid

water is available for hail growth. It is possible that some of these drops freeze, start riming, and then grow to hail by accretion. On the other hand, the drops might be accreted by hailstones already present aloft.

Six minutes later, the microphysical structure has changed distinctly (Fig. 17). The extent of the rain region has largely decreased, while the hail signature has increased due to a drastically increased LDR (up to -6 dB), a maximum being located at 7 km AGL ($-20°$ to $-25°$C). As these very high LDR values do not decrease with time, we are led to conclude that they are mainly caused by highly irregular hailstones possibly having a lobe structure that is basically maintained during fallout to the ground. It seems improbable that the high LDR is caused by wetting alone as with decreasing LWC the accreted water should freeze at the low temperatures to which the hailstones are exposed. Some of the hail seems to have penetrated downward into the rain region, thus progressively filling the weak echo region and causing it to collapse, at least in those parts closest to the main precipitation shaft. But this precipitation outbreak does not cause the
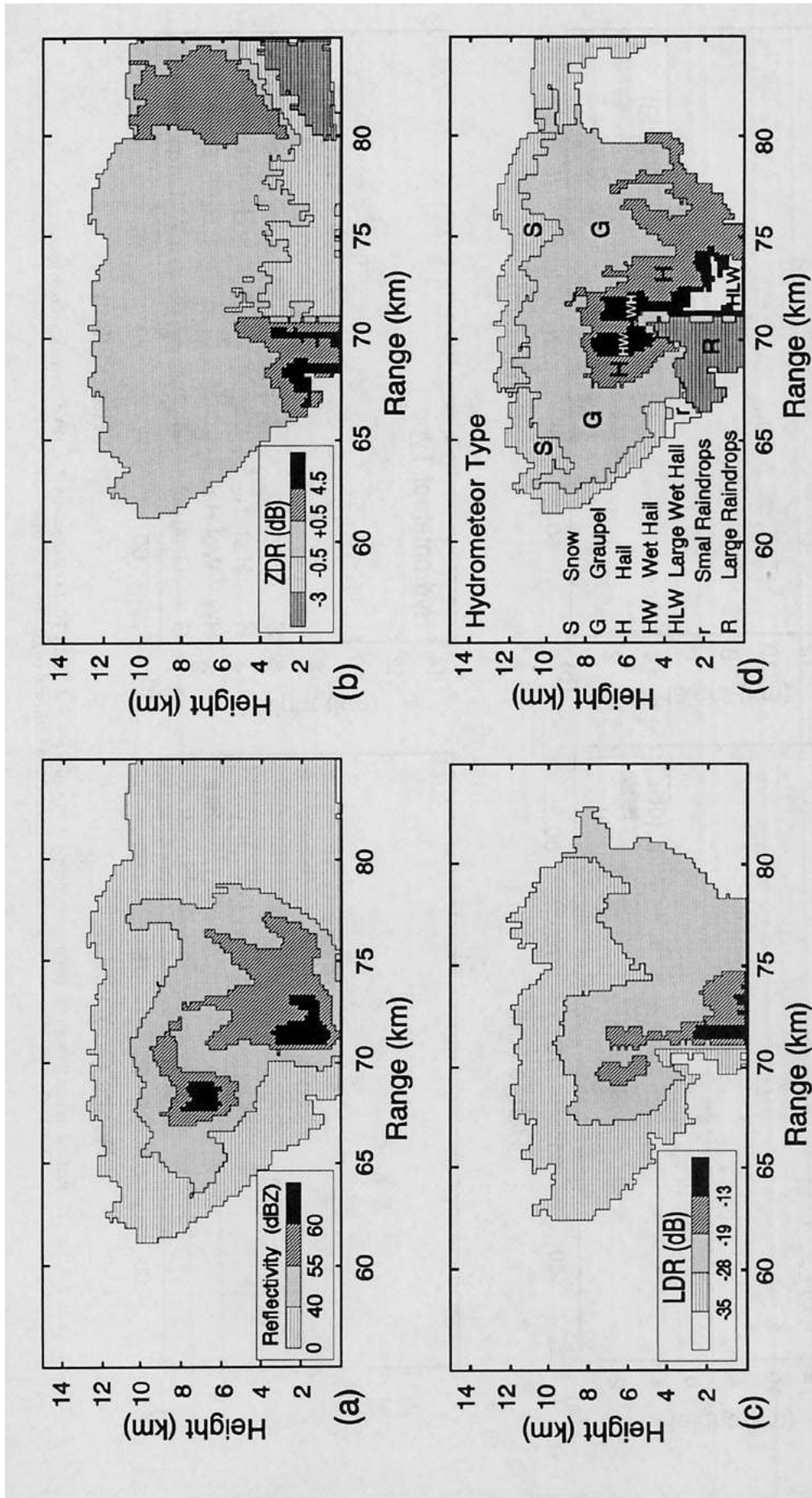
Fig. 16. Vertical section through the storm's core during its vigorous phase at 1414 UTC. (a) Reflectivity Z_{HH}, (b) differential reflectivity Z_{DR}, (c) linear depolarization ratio LDR, and (d) hydrometeor type.
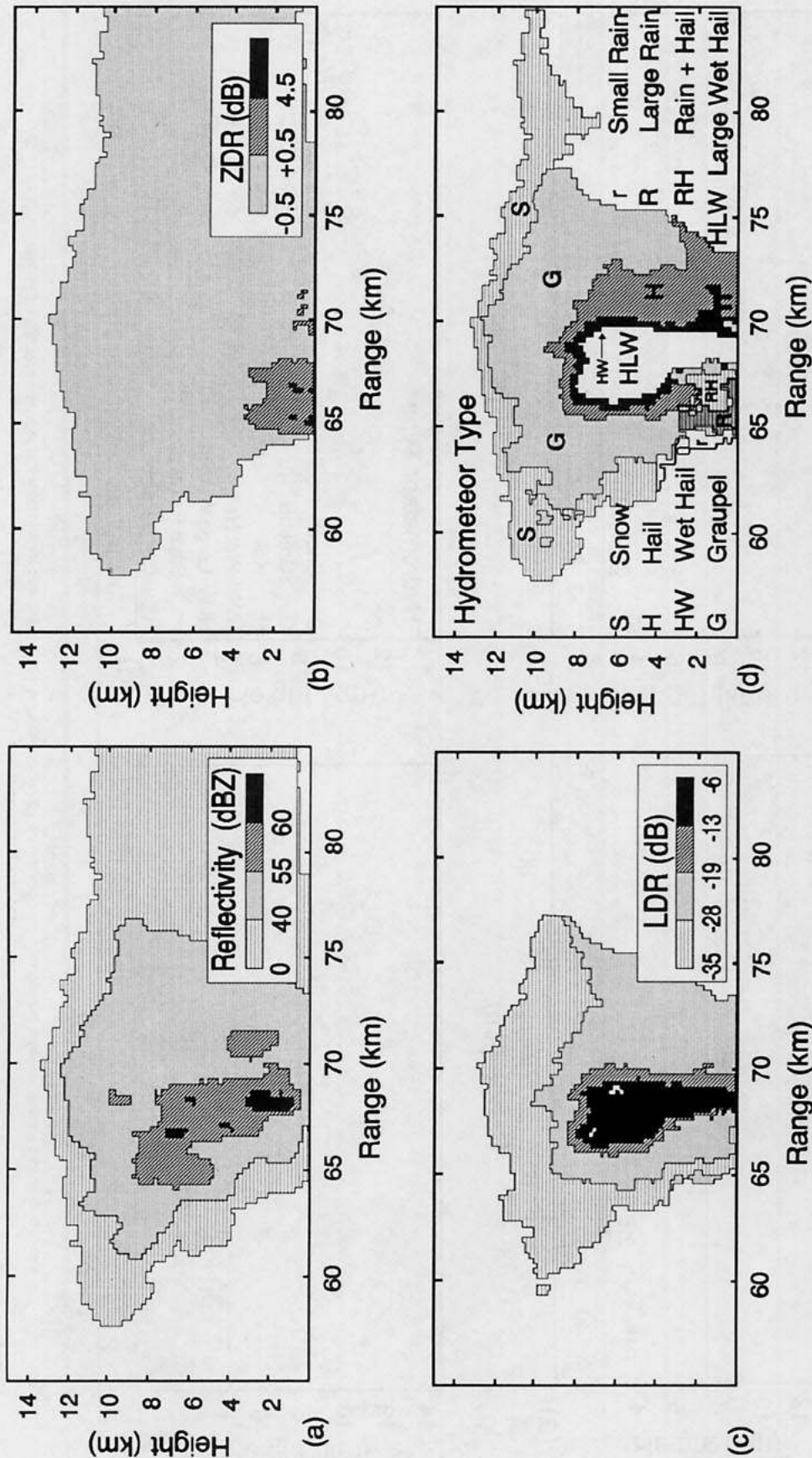
FIG. 17. Vertical section through the storm's core during its vigorous phase at 1420 UTC. (a) Reflectivity Z_{HH}, (b) differential reflectivity Z_{DR}, (c) linear depolarization ratio LDR, and (d) hydrometeor type.

WER to vanish completely; it only causes a more or less unsteadiness in its location relative to the storm.

9. Summary and conclusions

In this paper, a special type of hailstorm, the V-shaped storm (so called because of the V-shaped low- and midlevel reflectivity structures), was discussed from a dynamical as well as microphysical point of view. The storm developed in an environment characterized by a Richardson number in the intermediate range between the supercell and multicell regime. Consequently, properties from both types of storms were combined here.

The propagation of the storm was to the right of the shear and a weak echo region was present permanently even though it had a nonstationary character. New cells developed at the southern edge of the storm and then traveled around the western and eastern storm flanks. Those particles passing directly over the WER could grow into large hail that fell out directly beside the main updraft region associated with the main downdraft (Fig. 14a). The V echo seemed to be caused by the updraft zone, which was also V shaped. Embedded into this pattern was the main downdraft, coincident with the maximum reflectivity core. A pronounced mesocyclone could not be detected even though smaller regions of cyclonic rotation were present occasionally. The updraft itself showed sustained (location and shape) as well as transient features (long- and short-term variations).

As far as the microphysical processes are concerned, the classification of hydrometeors was possible by the polarimetric measurements. Especially, LDR and Z_{DR} proved to be useful for hail detection. Good agreement with ground-based observations was found. It was shown that accumulation zones of large drops associated with the high-reflectivity zones aloft were never present in the storm considered. The hydrometeors in these regions were graupel or hail particles grown either by riming of ice crystals or from frozen drops that did not survive long enough in the supercooled stage to contribute appreciably to the overhanging echo mass. The finding at least for this storm clearly falsifies the hypothesis of the existence of a large-drop zone, which was the base for several hail suppression experiments.

Nevertheless, raindrops have been a common feature in the main updraft zone of the storm. They were detected in the lower parts of the overhanging echo originating from melting graupel, in the WER as recirculated drops extending well into the supercooled region of the storm, and at the edge of the main precipitation shaft caused by size sorting of the melting particles in the horizontal wind field of the downdraft (see Fig. 14b).

The hydrometeor classification scheme proposed in this paper is somewhat empirical and needs to be con-

firmed by further numerical and observational studies. Nevertheless, it represents the state of the art of particle classification by polarimetric radar methods, and the results show consistency with storm dynamics. These kinds of measurements offer the only promising approach for detailed monitoring of precipitation formation processes within convective cloud complexes. As in situ observations inside hailstorms are difficult to obtain, ground-based data of hailfall as well as theoretical studies of the scattering behavior of model particles offer a good chance for verification of the proposed relationships.

REFERENCES

Aydin, K., and V. Giridhar, 1991: C-band dual polarization radar observables in rainfall: Implications on differentiating hydrometeor phase and estimating rainfall rate. Preprints, *25th Int. Conf. on Radar Meteorology,* Paris, Amer. Meteor. Soc., 670–673.

——, T. A. Seliga, and V. Balaji, 1986: Remote sensing of hail with a dual linear polarization radar. *J. Climate Appl. Meteor.,* **25,** 1475–1484.

——, ——, and Y. Zhao, 1991: Polarimetric C-band radar observables in melting hail: a computational study. Preprints, *25th Conf. on Radar Meteorology,* Paris, Amer. Meteor. Soc., 733–736.

Bailey, I. H., and W. C. Macklin, 1968: Heat transfer from artificial hailstones. *Quart. J. Roy. Meteor. Soc.,* **94,** 93–98.

Balakrishnan, N., and D. S. Zrnić, 1990a: Estimation of rain and hail rates in mixed-phase precipitation. *J. Atmos. Sci.,* **47,** 565–583.

——, and ——, 1990b: Use of polarization to characterize precipitation and discriminate large hail. *J. Atmos. Sci.,* **47,** 1525–1540.

Barnes, S. L., and C. W. Newton, 1986: Thunderstorms in the synoptic setting. *Thunderstorm Morphology and Dynamics,* E. Kessler, Ed., University of Oklahoma Press, 75–112.

Bringi, V. N., R. M. Rasmussen, and J. Vivekanandan, 1986a: Multiparameter radar measurements in Colorado convective storms. Part I: Graupel melting studies. *J. Atmos. Sci.,* **43,** 2545–2563.

——, J. Vivekanandan, and J. D. Tuttle, 1986b: Multiparameter radar measurements in Colorado convective storms. Part II: Hail detection studies. *J. Atmos. Sci.,* **43,** 2564–2577.

——, V. Chandrasekar, P. F. Meischner, J. Hubbert, and Y. Golestani, 1991: Polarimetric radar signatures of precipitation at S- and C-bands. *IEEE Proc.-F,* **138,** 109–119.

Browning, K. A., and R. Wexler, 1968: The determination of kinematic properties of a wind field using Doppler radar. *J. Appl. Meteor.,* **7,** 105–113.

——, and G. B. Foote, 1976: Airflow and hail growth in supercell storms and some implicaions for hail suppression. *Quart. J. Roy. Meteor. Soc.,* **102,** 499–533.

Changnon, S. A., 1970: Hailstreaks. *J. Atmos. Sci.,* **27,** 109–125.

Chisholm, A. J., and J. H. Renick, 1972: The kinematics of multicell and supercell Alberta hailstorms. *Alberta Hail Studies,* Research Council of Alberta Hail Studies, Rep. No. 72-2, 24–31.

English, M., and L. Cheng, 1984: Hailstone concentration and size at the ground and at the melting level: Variation of size distri-

bution in Alberta hailstorms. Preprints, *Ninth Int. Cloud Physics Conf.*, Tallinn, USSR, ICCP/IAMAP, 83–86.

Federer, B., A. Waldvogel, W. Schmidt, H. H. Schiesser, F. Hampel, M. Schweingruber, W. Stahel, J. Bader, J. F. Mezeix, N. Doras, G. D'Aubigny, G. DerMegreditchian, and D. Vento, 1986: Main results of Grossversuch IV. *J. Climate Appl. Meteor.*, **25**, 917–957.

Foote, G. B., 1985: Aspects of cumulonimbus classification relevant to the hail problem. *J. Rech. Atmos.*, **19**, 61–74.

——, and C. G. Wade, 1982: Case study of a hailstorm in Colorado. Part I: Radar echo structure and evolution. *J. Atmos. Sci.*, **39**, 2828–2846.

——, and H. W. Frank, 1983: Case study of a hailstorm in Colorado. Part III: Air-flow from triple-Doppler measurements. *J. Atmos. Sci.*, **40**, 686–707.

Fovell, R. G., and Y. Ogura, 1989: Effect of vertical wind shear on numerically simulated multicell storm structure. *J. Atmos. Sci.*, **46**, 3144–3176.

Heymsfield, A. J., and D. J. Musil, 1982: Case study of a hailstorm in Colorado. Part II: Particle growth processes at mid-levels deduced from in-situ measurements. *J. Atmos. Sci.*, **39**, 2847–2866.

Höller, H., 1983: Detailed and parameterized modeling of cloud-microphysics in a stationary cloud model. *Meteor. Rdsch.*, **36**, 152–154.

——, 1986: Simulation of cloud-microphysical development in the updraft region of a mixed phase cloud. Rep. Int. Cloud Modelling Workshop/Conf., Irsee, FRG. WMO/TD-No. 139, 163–175.

Hoinka, K. P., and F. Rösler, 1987: The surface layer on the leeside of the Alps during Foehn. *Meteor. Atmos. Phys.*, **37**, 245–258.

Jameson, A. R., and D. B. Johnson, 1990: Cloud microphysics and radar. *Radar in Meteorology*, D. Atlas, Ed., Amer. Meteor. Soc., 323–340.

Knight, C. A., G. B. Foote, and P. W. Summers, 1979: Results of a randomized hail suppression experiment in Northeast Colorado. Part IX: Overall discussion and summary in the context of physical research. *J. Appl. Meteor.*, **18**, 1629–1639.

Knight, N. C., 1986: Hailstone shape factors and its relation to radar interpretation of hail. *J. Climate Appl. Meteor.*, **25**, 1956–1958.

Meischner, P. F., 1990: Cloud dynamics and cloud microphysics by radar measurements. *Remote Sensing and the Earth's Environment*. Proceedings of Alpbach, Austria. ESA SP-301, 19–26.

——, V. N. Bringi, D. Heimann, and H. Höller, 1991: A squall line in southern Germany: Kinematics and precipitation formation as deduced by advanced polarimetric and Doppler radar measurements. *Mon. Wea. Rev.*, **119**, 678–701.

Nelson, S. P., 1987: The hybrid multicellular-supercellular storm—an efficient hail producer. Part II: General characteristics and implications for hail growth. *J. Atmos. Sci.*, **44**, 2042–2059.

——, and N. C. Knight, 1987: The hybrid multicellular-supercellular storm—an efficient hail producer. Part I: An archetypal example. *J. Atmos. Sci.*, **44**, 2042–2059.

Pitter, R. L., and H. R. Pruppacher, 1973: A wind tunnel investigation of freezing of small water drops falling at terminal velocity in air. *Quart. J. Roy. Meteor. Soc.*, **99**, 540–550.

Pruppacher, H. R., and J. D. Klett, 1978: *Microphysics of Clouds and Precipitation*. Reidel, 714 pp.

Rasmussen, R. M., and A. J. Heymsfield, 1987a: Melting and shedding of graupel and hail. Part I: Model physics. *J. Atmos. Sci.*, **44**, 2754–2763.

——, and ——, 1987b: Melting and shedding of graupel and hail. Part II: Sensitivity study. *J. Atmos. Sci.*, **44**, 2764–2782.

Schroth, A. C., M. S. Chandra, and P. F. Meischner, 1988: A C-band coherent polarimetric radar for propagation and cloud physics research. *J. Atmos. Oceanic Technol.*, **5**, 803–822.

Seliga, T. A., and V. N. Bringi, 1976: Potential use of radar differential reflectivity measurements at orthogonal polarizations for measuring precipitation. *J. Appl. Meteor.*, **15**, 69–76.

Steinhorn, I., and D. S. Zrnić, 1989: Differential propagation constant and differential reflectivity characterize rain and hail in high reflectivity regions. Preprints, *24th Conf. on Radar Meteorology*, Tallahassee, Amer. Meteor. Soc., 367–370.

Sulakvelidze, G. K., 1969: *Rainstorms and Hail*. Israel Program for Sci. Transl., Jerusalem, 310 pp.

Vivekanandan, J., V. N. Bringi, and R. Raghavan, 1990: Multiparameter radar modeling and observations of melting ice. *J. Atmos. Sci.*, **47**, 549–564.

Waldvogel, A., L. Klein, D. J. Musil, and P. L. Smith, 1987: Characteristics of radar-identified big drop zones in Swiss hailstorms. *J. Climate Appl. Meteor.*, **26**, 861–877.

Weisman, M. L., and J. B. Klemp, 1982: The dependence of numerically simulated convective storms on vertical wind shear and buoyancy. *Mon. Wea. Rev.*, **110**, 504–520.

Zrnić, D. S., 1987: Three-body scattering produces precipitation signature of special diagnostic value. *Radio Sci.*, **22**, 76–86.